

AD-A071 796

DYNAMICS TECHNOLOGY INC TORRANCE CA

F/G 20/4

GENERATION RATE OF TURBULENT PATCHES IN THE LAMINAR BOUNDARY LA--ETC(U)

JUN 79 C P CHEN, Y GOLAND, E RESHOTKO

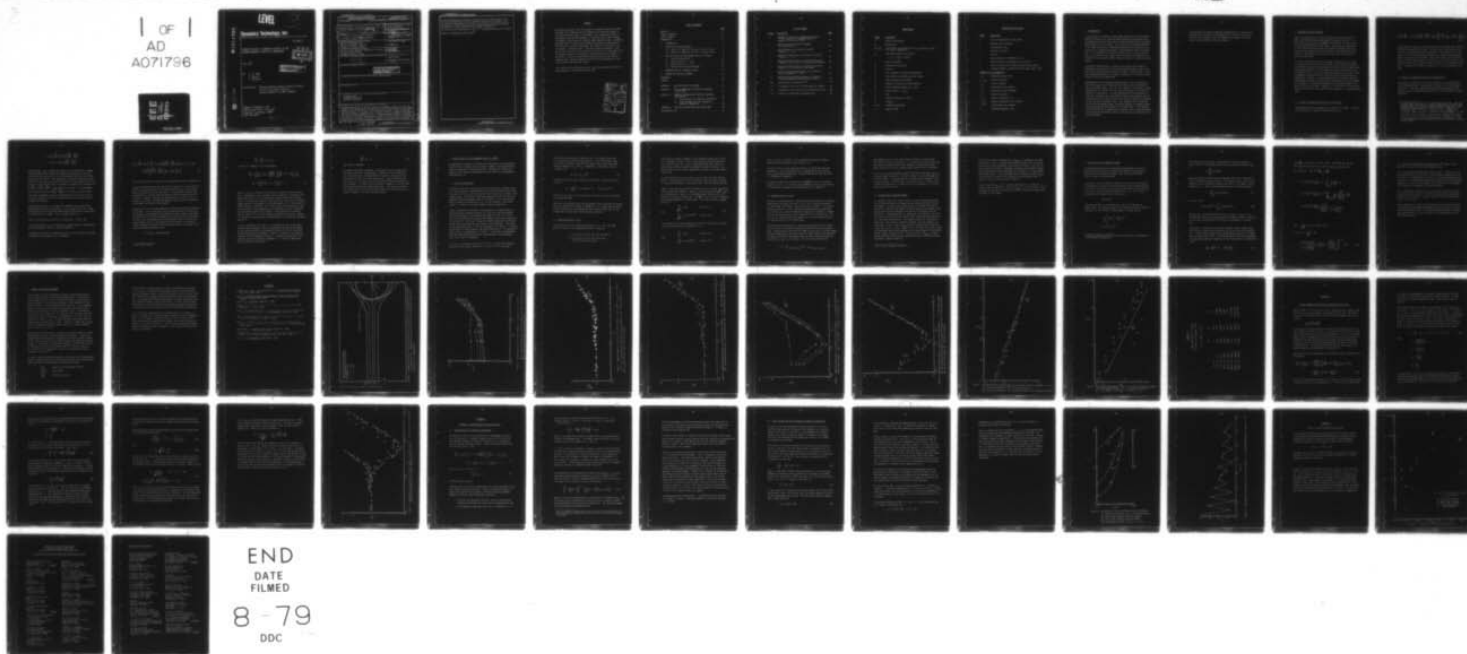
N00014-77-C-0005

UNCLASSIFIED

DT-7802-9

NL

| OF |
AD
A071796





NATIONAL BUREAU OF STANDARDS
MICROCOPY RESOLUTION TEST CHART

LEVEL

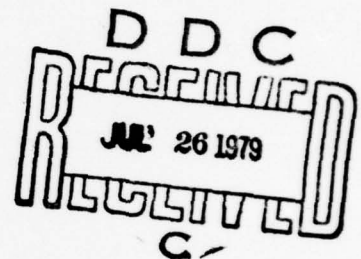
12

AD A071796

Dynamics Technology, Inc.

DT-7802-9

GENERATION RATE OF TURBULENT PATCHES IN THE
LAMINAR BOUNDARY LAYER OF A SUBMERSIBLE



JUNE 1979

This document has been approved
for public release and sale; its
distribution is unlimited.

By: C. P. CHEN
Y. GOLAND
E. RESHOTKO

SUPPORTED BY: DEFENSE ADVANCED RESEARCH PROJECTS AGENCY
AND OFFICE OF NAVAL RESEARCH
CONTRACT N00014-77-C-0005 (P00003)

DDC FILE COPY

DYNAMICS TECHNOLOGY, INC.
3838 CARSON STREET, SUITE 110
Torrance, CALIFORNIA 90503
(213) 540-5557

79 06 27 006

REPORT DOCUMENTATION PAGE		READ INSTRUCTIONS BEFORE COMPLETING FORM
1. REPORT NUMBER	2. GOVT ACCESSION NO.	3. RECIPIENT'S CATALOG NUMBER
4. TITLE (and Subtitle) Generation Rate of Turbulent Patches in the Laminar Boundary Layer of a Submarine <u>Submersible</u>		5. TYPE OF REPORT & PERIOD COVERED Technical Report
7. AUTHOR(s) C. P. /Chen, Y. /Goland and E. Reshotko		6. PERFORMING ORG. REPORT NUMBER DT-7802-9
9. PERFORMING ORGANIZATION NAME AND ADDRESS Dynamics Technology, Inc. 3838 Carson Street, Suite 110 Torrance, California 90503		8. CONTRACT OR GRANT NUMBER(s) Contract N00014-77-C-0005 (P00003)
11. CONTROLLING OFFICE NAME AND ADDRESS Office of Naval Research, Department of the Navy 800 North Quincy Street Arlington, Virginia 22217		10. PROGRAM ELEMENT, PROJECT, TASK AREA & WORK UNIT NUMBERS NR 062-565
14. MONITORING AGENCY NAME & ADDRESS (if different from Controlling Office) <u>1254 P.I.</u>		12. REPORT DATE 11 June 1979
		13. NUMBER OF PAGES
		15. SECURITY CLASS. (of this report) UNCLASSIFIED
		15a. DECLASSIFICATION/DOWNGRADING SCHEDULE
16. DISTRIBUTION STATEMENT (of this Report) <div style="border: 1px solid black; padding: 5px; text-align: center;">This document has been approved for public release and sale; its distribution is unlimited.</div>		
17. DISTRIBUTION STATEMENT (of the abstract entered in Block 20, if different from Report)		
18. SUPPLEMENTARY NOTES		
19. KEY WORDS (Continue on reverse side if necessary and identify by block number) Turbulent Patch Suspended Particulate Particle Trajectory		
20. ABSTRACT (Continue on reverse side if necessary and identify by block number) Suspended particulate in the environment of underwater vehicles has been suspected to be responsible for the generation of turbulent patches in the laminar boundary layer of the vehicle. This speculation, which is supported by much indirect evidence, is examined in this report through an attempt at calculating the turbulent patch generation rate. The method presented herein is based on the premise that patches are generated by those particles entering the boundary layer that are sufficiently large to "trigger" a turbulent event. Since the		

393 134

UNCLASSIFIED

SECURITY CLASSIFICATION OF THIS PAGE(When Data Entered)

triggering mechanism is not known, the choice of a critical particle size will involve some empiricism. An important element of the method is the calculation of the number of particles of a given size and specific gravity that enter the laminar boundary layer, through computation of the particle trajectories in the inviscid flow field about the vehicle.

For a particle size distribution, $n(d) \sim d^{-p}$, the generation rate of turbulent patches is predicted to vary as $U_{\infty}^{p/2}$.

UNCLASSIFIED

SECURITY CLASSIFICATION OF THIS PAGE(When Data Entered)

ABSTRACT

Suspended particulate in the environment of underwater vehicles has been suspected to be responsible for the generation of turbulent patches in the laminar boundary layer of the vehicle. This speculation, which is supported by much indirect evidence, is examined in this report through an attempt at calculating the turbulent patch generation rate. The method presented herein is based on the premise that patches are generated by those particles entering the boundary layer that are sufficiently large to "trigger" a turbulent event. Since the triggering mechanism is not known, the choice of a critical particle size will involve some empiricism. An important element of the method is the calculation of the number of particles of a given size and specific gravity that enter the laminar boundary layer, through computation of the particle trajectories in the inviscid flow field about the vehicle.

For a particle size distribution, $n(d) \sim d^{-p}$, the generation rate of turbulent patches is predicted to vary as $U_{\infty}^{p/2}$.

Accession For	
NTIS GRA&I	
DDC TAB	
Unannounced	
Justification <i>Per file</i>	
By <i>on file</i>	
Distribution/	
Availability Codes	
Dist	Avail and/or special
<i>A</i>	

TABLE OF CONTENTS

	<u>PAGE</u>
ABSTRACT.	i
TABLE OF CONTENTS	ii
LIST OF FIGURES	iii
NOMENCLATURE.	iv
1. INTRODUCTION	1
2. EQUATIONS OF PARTICLE MOTION	3
2.1 Motion of a Spherical Particle in a Still Fluid.	3
2.2 Motion of a Spherical Particle in a Moving Fluid	4
3. PARTICLE ENTRY INTO THE BOUNDARY LAYER OF A SPHERE	9
3.1 Flowfield Description.	9
3.2 Capture Area for $s = 1.01$	10
3.3 Capture Area for $s > 1.01$	12
3.4 Maximum Relative Reynolds Number	13
4. GENERATION RATE OF TURBULENT PATCHES	15
5. SUMMARY AND CONCLUDING REMARKS	19
REFERENCES.	21
FIGURES	22
APPENDIX A: DRAG COEFFICIENT OF A SPHERE.	30
APPENDIX B: SCALING PARAMETERS FOR PARTICLE TRAJECTORY CALCULATIONS	31
APPENDIX C: NUMERICAL FORMULATION OF PARTICLE TRAJECTORY CALCULATION.	37
C.1 Considerations for Numerical Formulation.	37
C.2 Error Estimate and Time Increment of Numerical Computation	40
APPENDIX D: EFFECTS OF BASSET FORCE AND VIRTUAL MASS.	45
DISTRIBUTION LIST	47

LIST OF FIGURES

<u>FIGURE</u>	<u>DESCRIPTION</u>	<u>PAGE</u>
1.	Schematic of a Particle Trajectory Calculation in the Flowfield of a Submerged Sphere of Radius $a = 15.24$ cm (0.5 ft).	22
2.	Capture Area versus Particle Diameter as a Function of U_{∞}	23
3.	Capture Height as a Function of Particle Diameter, $s = 1.01$	24
4.	Normalized Capture Area as a Function of Particle Diameter, $s = 1.01$	25
5.	Normalized Capture Area as a Function of Particle Diameter $U_{\infty} = 15.24$ m/sec and Various Density Ratios . .	26
6.	Normalized Capture Area as a Function of Particle Diameter $s = 2.5$ and Various Flow Speeds	27
7.	Maximum Relative Reynolds Number as a Function of Particle Diameter, $s = 1.01$	28
8.	Maximum Relative Reynolds Number as a Function of Particle Diameter for Various Density Ratios.	29
B-1	Capture Area as a Function of $\gamma^{\frac{1}{2}}$	36
C-1	Percentage of Error for Different Numerical Methods. . .	43
C-2	Percentage of Error versus Initial Particle Location . .	44
D-1	Effects of Virtual Mass and Basset Force	46

NOMENCLATURE

<u>SYMBOL</u>	<u>DESCRIPTION</u>
a	radius of the sphere
A_c	capture area
A_1, A_2, A_3	coefficients in the definition of C_D ; numerical values are given in Appendix A
C_D	drag coefficients of the particle $C_D = A_1 + A_2 R_r^{-1} + A_3 R_r^{-2}$
d	particle diameter
g	acceleration of gravity
\hat{g}	(0,0,-g)
h	time increment in numerical computation
N	total number of particles per unit volume
P	static pressure of the fluid
p	exponent of particle size distribution
R_r	Relative Reynolds number, $R_r = u d/\nu$
s	density ratio, $s = \rho_p/\rho_f$
t	time
\bar{u}	relative velocity, $\bar{u} = \bar{V}_f - \bar{V}_p$
V	velocity
X,Y,Z	Cartesian coordinates
Y_c	capture height

NOMENCLATURE (Continued)

<u>SYMBOL</u>	<u>DESCRIPTION</u>
β	ratio of characteristic time scales
δ	boundary layer thickness
ϵ	percentage of error
ν	kinematic viscosity
ρ	density
τ	dummy variable in integration, time
ϕ	angular position with respect to stream axis
γ	ratio of fluid inertia forces to particle drag forces
ζ	distance between a streamline and the sphere when $\phi = 90^\circ$

SUBSCRIPTS and SUPERSSCRIPTS

$()_f$	pertaining to the fluid
$()_{i,j,k}$	tensorial quantity
$()_o$	initial condition
$()_p$	pertaining to the particle
$()_\infty$	pertaining to the freestream
$(\bar{ })$	vectorial quantity
$()^n$	quantity evaluated at t_n
$()^{(k)}$	quantity evaluated at kth iteration
$()^{(0)}$	initial guess for iteration
$()'$	normalized quantity, $\sim 0(1)$

1. INTRODUCTION

In the testing of underwater vehicle models designed to sustain extended regions of laminar flow, there have been numerous instances where drag perturbations have been seen as well as other manifestations of turbulent patches passing over the models. The origin of these turbulent patches is not known, but there is considerable speculation that they may be attributable to suspended particulate in the underwater vehicle's environment. It is important to pursue this matter since all vehicle environments, including the ocean, contain particulate that can therefore be of consequence to drag, heat transfer and other aspects of laminar flow technology.

The method presented herein is based on the premise that patches are generated by those particles entering the laminar boundary layer of the vehicle that are sufficiently large to trigger a turbulent event. Since the triggering mechanism is not known, the choice of a critical particle size will involve some empiricism.

Implementation of this procedure requires that, first, an estimate be made of the rates at which particles of different sizes and densities enter the boundary layer. This, in turn, requires a calculation of their trajectories, as a function of their size and density, in the inviscid flowfield of the vehicle. For each combination of size and density, a "limiting" trajectory that just grazes the edge of the boundary layer is identified and all particles within that limiting trajectory are assumed to enter the vehicle boundary layer. The ingestion rate of particles into the vehicle boundary layer can then be obtained by integrating over the size and density distributions of the particulate. If one assigns an efficiency factor for generating a turbulent event to each combination of particle size and density, then the turbulent patch generation rate can be estimated.

The trajectory calculation procedures presented herein, of course, are applicable to any situation that depends on the ingestion rate of particulate into a boundary layer; for example, the clogging of suction slots or porous surfaces, or surface erosion.

2. EQUATIONS OF PARTICLE MOTION

When a suspended particle is moving relative to a surrounding fluid, there are several different hydrodynamic forces which act on it. In this study, all particles are assumed to be spherical in order to simplify the determination of these forces. Also, since our interest is in the limiting trajectories that just graze the boundary layer, the particles are assumed to be at a sufficiently large distance from the vehicle so that boundary layer and wall corrections to the particle motion are negligible.

Particle trajectories have been calculated for heavy particles moving in a gaseous flow field (Morsi & Alexander (1972) and Michael (1968)). In their derivations of the equations of particle motion, unsteady forces were neglected because of the extremely high value of the particle-to-fluid density ratio. For nearly neutrally buoyant particles, all of the hydrodynamic forces which act on the particle should be considered in determining its motion. In the limited amount of available literature, the equation of motion of the particle is not always correctly presented. We, therefore, will develop the complete particle motion equation in a moving fluid in this report. However, it is instructive in the development to consider first the case of particles moving in a quiescent ambient fluid.

2.1 Motion of a Spherical Particle in a Still Fluid

A good account of this classical work is given by Yih (1969). The equation of motion for a particle starting from rest is

$$\frac{\pi}{6} d^3 \rho_p \frac{dv_p}{dt} = - \frac{\pi}{4} \rho_f d^3 \left\{ \frac{1}{3} \frac{dv_p}{dt} + \frac{12v_p}{d^2} + \frac{6}{d} \left(\frac{v}{\pi} \right)^{\frac{1}{2}} \int_0^t \frac{dv_p}{dt} \frac{d\tau}{(t-\tau)^{\frac{1}{2}}} + \frac{2}{3} \left(1 - \frac{\rho_p}{\rho_f} \right) g \right\} \quad (1)^*$$

In the present situation, each particle moves in a straight line in the direction of the gravitational force. The terms on the right hand side are, in order: the force caused by the particle's "virtual mass" (i.e., the inertia of the fluid surrounding the particle); viscous drag according to Stokes' law; the so-called "Basset" force, which relates to the time history of the past acceleration of the particle; and the buoyancy force. Note that the virtual mass is $\frac{\pi}{12} d^2 \rho_f$, exactly the same as for irrotational motion. The analytical solution of equation (1) is also presented in Yih's book.

2.2 Motion of a Spherical Particle in a Moving Fluid

The extension of equation (1) to particle motion in a non-uniform flow is not straightforward. The principal difficulty lies in the acceleration terms. It has been established analytically by Symington (1978) that for an inviscid non-uniform flowfield, the forces acting on a moving sphere are

* This equation is valid only for a low Reynolds number flow. Odar and Hamilton (1964) found that for a sphere undergoing rectilinear, simple harmonic motion up to $R_r=62$, an equation similar to equation (1) describes the sphere motion well if the drag force is taken to be $\frac{\pi}{8} \rho_f d^2 C_D v_p^2$, where $C_D = C_D(R_r)$. Furthermore, when $v_p^2 / \left(\frac{dv_p}{dt} \right) d \ll 0.1$, the coefficients for the virtual mass inertial force ($\frac{1}{3} dv_p/dt$) and Basset force (the integral term) are the same as those in equation (1). This extension applied to free-fall sphere motion was experimentally verified by Odar (1966).

$$\begin{aligned}\bar{F} &= \frac{\pi}{6} d^3 \rho_f \frac{D\bar{V}_f}{Dt} + \frac{\pi}{12} d^3 \rho_f \left[\frac{D\bar{V}_f}{Dt} - \frac{d\bar{V}_p}{dt} \right] \\ &= -\frac{\pi}{6} d^3 \nabla p + \frac{\pi}{12} d^3 \rho_f \left[\frac{D\bar{V}_f}{Dt} - \frac{d\bar{V}_p}{dt} \right],\end{aligned}$$

where $\frac{D}{Dt} = \frac{\partial}{\partial t} + (\bar{V}_f \cdot \nabla)$ and $\frac{d}{dt} = \frac{\partial}{\partial t} + (\bar{V}_p \cdot \nabla)$ are the time rates of change along a streamline and a particle trajectory, respectively. The first term on the right hand side is due to the pressure gradient in the fluid surrounding the particle. The second term is the force required to accelerate the virtual mass of the particle relative to the ambient fluid. Comparison of this term with that in equation (1) suggests the replacement of $\left(-\frac{d\bar{V}_p}{dt}\right)$ by $\left(\frac{D\bar{V}_f}{Dt} - \frac{d\bar{V}_p}{dt}\right)$ in a non-uniform flow field. This replacement has often been taken to be $\left(\frac{d\bar{V}_f}{dt} - \frac{d\bar{V}_p}{dt}\right)$, for instance, see Hinze (1959). The latter replacement suggests the hydrodynamic force arising from the relative acceleration is in the direction of particle trajectory, which we regard as erroneous.

Another generalization is to extend the treatment of the viscous drag force beyond the Stokes' flow regime, since we expect that, for a large and dense particle, the Reynolds number based on the relative motion could be of order unity or larger. Thus, the generalization is,

$$\text{Viscous force acting on the particle} = \frac{\pi}{8} d^2 C_D \rho_f |\bar{V}_f - \bar{V}_p| (\bar{V}_f - \bar{V}_p)$$

The drag coefficient, C_D , as a function of Reynolds number as presented by Morsi and Alexander (1972), is given in Appendix A.

The equation of motion of a spherical particle in a non-uniform flow field as generalized from equation (1) is therefore

$$\begin{aligned} \frac{\pi}{6} d^3 \rho_p \frac{d\bar{V}_p}{dt} = & \frac{\pi}{6} d^3 \rho_f \frac{D\bar{V}_f}{Dt} + \frac{\pi}{4} \rho_f d^3 \left\{ \frac{1}{3} \left(\frac{D\bar{V}_f}{Dt} - \frac{d\bar{V}_p}{dt} \right) + \frac{C_D}{2d} |\bar{V}_f - \bar{V}_p| (\bar{V}_f - \bar{V}_p) \right. \\ & \left. + \frac{6}{d} \left(\frac{\nu}{\pi} \right)^{\frac{1}{2}} \int_0^t \left(\frac{D\bar{V}_f}{Dt} - \frac{d\bar{V}_p}{dt} \right) \frac{d\tau}{(t-\tau)^{\frac{1}{2}}} + \frac{2}{3} \left(1 - \frac{\rho_p}{\rho_f} \right) \hat{g} \right\}. \end{aligned} \quad (2)^*$$

Terms inside the braces in equation (2) correspond to those in equation (1).

A major assumption made in the derivation of equation (2) to describe the motion of a spherical particle is that the particle size is much smaller than the length scale of the flow field. This assumption excludes applying equation (2) when the particle enters the laminar boundary layer of a vehicle. However, since only the capture rate of particles is of interest in this study, the detailed trajectory after a particle penetrates the boundary layer edge is not necessary.

Equation (2) is to be solved numerically to obtain a particle's trajectory and velocity. For a given body, the surrounding potential flowfield and the boundary layer thickness are presumed to be known either analytically or numerically. Since \bar{V}_p is expected to be quite close to \bar{V}_f , the numerical error in solving equation (2) could be quite large if it were to be solved directly for \bar{V}_p . The accuracy would be higher if the relative velocity between the particle and the fluid were solved for instead. Defining the relative velocity to be

$$\bar{u} \equiv \bar{V}_f - \bar{V}_p, \text{ and noting that}$$

* See footnote, page 3.

$$\frac{D\bar{V}_f}{Dt} = \frac{d\bar{V}_f}{dt} + (\bar{u} \cdot \nabla) \bar{V}_f ,$$

equation (2) becomes, after rearrangement,

$$\begin{aligned} \frac{d\bar{u}}{dt} + \frac{3C_D}{2(2s+1)d} |\bar{u}| \bar{u} + \frac{18\sqrt{\nu/\pi}}{(2s+1)d} \int_0^t \left[\frac{d\bar{u}}{d\tau} + (\bar{u} \cdot \nabla) \bar{V}_f \right] \frac{d\tau}{(t-\tau)^{1/2}} \\ + \left(\bar{u} - \frac{2(s-1)}{2s+1} \bar{V}_f \right) \cdot \nabla \bar{V}_f + \frac{2(s-1)}{2s+1} \hat{g} = 0 , \end{aligned} \quad (3)$$

where $s = \rho_p/\rho_f$ is the ratio of the particle's density to the fluid density. The meaning of the individual terms in equation (3) should be self-explanatory by now. This is a nonlinear integro-differential equation. With $s = 1$, the trivial solution $\bar{u} = 0$ exists; this implies that a neutrally buoyant particle, even though it is not deformable as is a fluid particle, always follows a streamline. This trivial solution has served as a check for the numerical code developed to solve equation (3) and as a baseline for choosing the proper time increment. The integrand of the "Basset" term is singular at $\tau = t$, which poses some numerical difficulty. However, the integral is bounded because the denominator of the integrand approaches zero as $t^{-1/2}$.

As seen from equation (3), when $s \gg 1$, the effects of the virtual mass, viscous drag and "Basset" force are negligible, and the rate of change of the relative velocity is balanced by the inertial force of the fluid and the gravitational acceleration. When s is of order 1, all terms are important in the trajectory calculation. The scaling parameters of the particle motion are discussed in Appendix B. In order to compute the particle position, the relation

$$\frac{d\bar{x}_p}{dt} = \bar{V}_f - \bar{u} \quad (4)$$

must also be integrated.

For reasons explained in Appendix C, equations (3) and (4) were solved separately rather than simultaneously. Equation (3) was solved by an improved Euler method. Various methods of solving equation (4) have been tested for their efficiency and accuracy: these include explicit and improved Euler methods, and 4th and 6th order Hamming predictor-corrector methods. For reasons to be explained in Appendix C, the 4th order Hamming predictor-corrector method was chosen. The numerical solution was obtained using a Cartesian coordinate system and the details are reported in Appendix C for any interested readers.

3. PARTICLE ENTRY INTO THE BOUNDARY LAYER OF A SPHERE

To demonstrate our method of estimating the generation rate of turbulent patches within a boundary layer, we chose a sphere as the submersible because its flowfield is known analytically. Although the results for a sphere are not necessarily applicable to other vehicles, the methodology developed here, is.

3.1 Flow Field Description

To determine the entry rate of particles into the sphere's boundary layer, it is only necessary to determine the cross-sectional area enclosed in the free stream by those particle trajectories which just graze the edge of the boundary layer. All particles that pass through that cross section will eventually enter the boundary layer of the sphere. This cross-sectional area is termed the "capture area", A_c , and its boundary, "the capture height", Y_c , which is the radial distance from the stream axis.

Figure 1 describes the features of the computation of capture height, Y_c . For near-neutrally bouyant particles ($s=1.01$) the limiting trajectory tends to be tangent to the boundary layer edge at $\phi = 90^\circ$. For $s=2.5$, the limiting trajectory often grazes the boundary layer edge at some angle ϕ less than 90° . The larger the particle density the more the turning of the particle trajectory lags the turning of the streamlines. The origin of the coordinate system is fixed at the center of the sphere: X is along the direction of the horizontal free stream velocity, U_∞ ; Y is opposite to gravity; and Z is perpendicular to X and Y . To simplify the computation only the fluid and particle motion in the meridional plane containing both X and Y axes is considered

The radius of the sphere is 15.24 cm (0.5 ft). The particle trajectory calculations were always started at $X = -1.52$ m (-5.0 ft), and each

trajectory was calculated to impact or to $X = 0$, whichever came first. It is obvious that there are two values of Y - one for particles which go up over the sphere and the other for which they go below the sphere. These are denoted as Y_{c1} and Y_{c2} , respectively. The capture area, A_c , is taken to be

$$A_c = \frac{\pi}{4} (Y_{c1} - Y_{c2})^2 \quad (5)$$

The laminar boundary layer thickness on the sphere is determined by the relation

$$\delta(\phi) = \sqrt{\frac{av}{U_\infty}} (1.5 + .000119 \cdot \phi^2), \quad 0^\circ \leq \phi(\text{deg}) \leq 90^\circ$$

which is an empirical fit of the results of the series solution presented by Schlichting (1968).

The effect of the Basset force and the apparent mass on the particle trajectories is assessed and reported in Appendix D. It is found that the exclusion of those terms in the computation can introduce large errors in the trajectories of large near-neutrally bouyant particles.

3.2 Capture Area for $s = 1.01$

The capture area was calculated for particles of $s = 1.01$, with eight particle sizes and five freestream velocities. They are:

$$\begin{aligned} d &= 10, 30, 50, 75, 100, 175, 225, \text{ and } 300 \text{ } \mu\text{m}, \\ U_\infty &= 3.05, 6.10, 9.14, 12.19, 15.24 \text{ m/sec} \\ &\quad (10, 20, 30, 40, 50 \text{ ft/sec}) \end{aligned}$$

The results are shown in Figure 2. At a constant velocity, A_c is relatively constant for small particle sizes, then increases monotonically with larger particle size. This is expected because small particles, more or less, follow a streamline, whereas for larger particles, it is more difficult for the flow to change their courses, so a larger capture area results.

For small particle sizes, the value of A_c is larger for lower velocity which is a manifestation of the fact that the laminar boundary thickness is inversely proportional to the square root of the free stream velocity.

Figure 3 shows the capture height on either side of the center streamline versus the particle diameter. Values of Y_c are normalized by $\sqrt{a\delta}$, while d is normalized by δ where δ is the boundary layer thickness at $\phi = 90^\circ$. Within the accuracy of computation $Y_c / \sqrt{a\delta}$ versus d/δ can be fitted by two straight segments on a log-log plot. The relation between $Y_c / \sqrt{a\delta}$ and d/δ is:

$$\begin{aligned} \frac{Y_c}{\sqrt{a\delta}} &= 1.82 && \text{for } d/\delta < 0.4 \quad , \\ \text{and} &&& \\ \frac{Y_c}{\sqrt{a\delta}} &= 3.3 (d/\delta)^{0.65} && \text{for } d/\delta > 0.4 \quad . \end{aligned} \tag{6}$$

The corresponding relation between the normalized capture area, $A_c / \pi a \delta$ and the normalized particle diameter d/δ is:

$$\begin{aligned} \frac{A_c}{\pi a \delta} &= 3.31 && \text{for } d/\delta < 0.4 \quad , \\ \text{and} &&& \\ \frac{A_c}{\pi a \delta} &= 10.9 (d/\delta)^{1.3} && \text{for } d/\delta > 0.4 \quad . \end{aligned} \tag{7}$$

which is plotted in Figure 4. For a particle that exactly follows a streamline, the theoretical value of $A_c/\pi a \delta$ is 3.

The use of the fit of the numerical data for Y_c , rather than the data themselves, is to minimize the effect of computation errors, since Y_{c1} and Y_{c2} were computed separately. The justification for scaling d with δ is developed in Appendix B.

It should be noted that the deviation of $A_c/\sqrt{\pi a \delta}$ for $d/\delta < 0.4$ from the theoretical value, 3, is primarily the consequence of the discrete nature of the numerical procedure as described more fully in Appendix C.

3.3 Capture Area for $s > 1.01$

In order to simulate testing in the particulate environment of a tow basin, capture areas for particles with $s = 1.5, 2$, and 2.5 were calculated at $U_\infty = 15.24$ m/sec (50 ft/sec). Results are shown in Figure 5. In contrast with the results for $s = 1.01$, the capture area decreases with particle size for $d/\delta < 0.2$, and the difference in magnitude is substantial between A_c 's for different density ratios, especially $s \neq 1.01$ and the rest. For $d/\delta > 0.2$, A_c increases with d and seems to fall on one straight line for all density ratios s on the log-log plot.

The validity of the definition of capture area (equation (5)) for higher density ratios is verified by computing the width of the actual capture area. The deviation of the ratio of height to width from 1 (circular shape) may conceivably arise from the gravitational force acting on the particles. To compute the width of the capture area, we simply eliminate gravity in computing Y_{c1} ($Y_{c2} = Y_{c1}$, of course). The ratio of height to width

$$\left| Y_{c1} - Y_{c2} \right|_{\text{with gravity}} / \left| Y_{c1} - Y_{c2} \right|_{\text{without gravity}}$$

was computed for $s = 2.5$, $U_{\infty} = 3.05$ m/sec (10 ft/sec) and 15.24 m/sec (50 ft/sec), $d = 30, 175$, and $300 \mu\text{m}$. It is practically unity indicating that the gravitational force is not important in determining A_c and, hence, the use of A_c for all density ratios studied here is justified.

For $s = 2.5$, A_c was calculated for other free stream velocities; the results are shown in Figure 6. Similar to Figure 5, $A_c/\pi a \delta$ decreases with d/δ first before it increases and then collapses onto a straight line on the log-log plot. As with Figure 5, $A_c/\pi a \delta$ for $s \geq 1.5$ is found to have a power-law dependence on d/δ when $d/\delta > 0.2$; the exponent is 1.7 in contrast with 1.3 for $s = 1.01$.

3.4 Maximum Relative Reynolds Number

In a potential flow, the inertial force of a fluid element moving along a curvilinear streamline is balanced by the pressure gradient acting on the element. For any particle whose density is different from that of the fluid, relative motion between the particle and the surrounding fluid results from the force imbalance; and the particle deviates from the streamline. A Reynolds number, R_r , defined by the magnitude of the relative velocity and the particle diameter helps to determine the nature of the flow about that particle. This Reynolds number was calculated at each point on the particle trajectory; however, only the maximum R_r is shown here. Figure 7 shows $(R_r)_{\max}$ along the trajectories of those particles past Y_{c1} for $s = 1.01$. Except for $U_{\infty} = 3.05$ m/sec (10 ft/sec), where the data become questionable because of the large tolerance* in the computation, $(R_r)_{\max}$ varies as $(d/\delta)^3$. When $(d/\delta) > 0.34$, $(R_r)_{\max}$ is always greater than one indicating that the generalization of drag force beyond the Stokes' regime is necessary.

* See the last paragraph of Appendix C.

For particles within the capture area, $(R_r)_{\max}$ is expected to be larger than shown in Figure 7, because the particles now go closer to the stagnation point and can experience larger relative velocity. Thus, the results presented in Figure 7 represent a maximum relative Reynolds number that a particle would experience along its trajectory if it just grazes the boundary layer. It was estimated from our computations that $(R_r)_{\max}$ for particles of a similar size but going into the boundary layer is about 2-3 times as large as shown in Figure 7.

Figure 8 shows $(R_r)_{\max}$ for all particle densities at $U_{\infty} = 50$ ft/sec. In contrast with the results for $s = 1.01$, $(R_r)_{\max}$ for $s \geq 1.5$ varies as $(d/\delta)^2$. No proper scaling has yet been found to further collapse the computed values shown in this figure.

4. GENERATION RATE OF TURBULENT PATCHES

The method presented here for estimating the generation rate of turbulent patches is based on the premise that patches are generated by those particles entering the boundary layer that are sufficiently large to trigger a turbulent event.

Assuming that the distribution of particles in the vehicle environment is homogeneous, the particle size distribution can be characterized by a single function $n(d)$, where $n(d)\Delta d$ is the total number of particles per unit volume within the diameter interval $(d, d+\Delta d)$. For a typical environment, the function $n(d)$ is taken to be

$$n(d) = Bd^{-p}$$

where the exponent p is evaluated from a best fit to tow tank or oceanic data. The unknown constant, B , is related to the total number of particles per unit volume, N , whose diameter is larger than d_m .

$$N = \int_{d_m}^{\infty} n(d)\Delta d^{\dagger} = \frac{B}{p-1} d_m^{1-p}$$

$$\therefore B = N(p-1) d_m^{p-1}$$

[†] Because of notational difficulties, the differential of d appearing in the integrand is denoted Δd .

Given the capture area, $A_c(d)$, for one density ratio, the total flux rate of particles of diameter greater than d_m entering the boundary layer is

$$U_\infty \int_{d_m}^{\infty} A_c(d) n(d) \Delta d .$$

Among those particles which enter the boundary layer, only a fraction of them will generate turbulent patches. This fraction, $\eta(d)$, which will be referred to as an "efficiency function" hereafter in this report, varies between 0 and 1. Then the total generation rate of turbulent patches is

$$F = U_\infty \int_{d_m}^{\infty} A_c(d) \eta(d) n(d) \Delta d . \quad (8)$$

With $n(d) = B d^{-p}$

$$F = N(p-1) d_m^{p-1} U_\infty \int_{d_m}^{\infty} A_c(d) \eta(d) d^{-p} \Delta d . \quad (8a)$$

Equation (8a) can be evaluated only if $\eta(d)$ is known. However, since the detailed mechanisms of the generation of turbulent patches by particles are not known, the evaluation of $\eta(d)$ will be approached in a simple way.

Considering a particle to be a moving roughness element suggests that the efficiency function should depend on the normalized particle diameter, d/δ . If one further assumes that turbulent patches occur only for large particles where $(d/\delta) > (d/\delta)_r$, then the generation rate can be estimated. The capture area defined in equation (7) for large particles is generalized to be

$$\frac{A_c}{\pi a \delta} \sim \left(\frac{d}{\delta} \right)^m \quad \text{for} \quad \left(\frac{d}{\delta} \right) > \left(\frac{d}{\delta} \right)_r , \quad (7a)$$

where $\left(\frac{d}{\delta}\right)_r = 0.4$ and $m = 1.3$ for $s = 1.01$. For simplicity, let the efficiency function be unity for $(d/\delta) > (d/\delta)_{\text{crit}}$ and zero for $d/\delta < (d/\delta)_{\text{crit}}$. Then, for $\left(\frac{d}{\delta}\right)_{\text{crit}} > \left(\frac{d}{\delta}\right)_r$

$$\begin{aligned} F &= (p-1)N d_m^{p-1} \left(\frac{A_c}{\pi a \delta}\right)_r U_\infty \pi a \delta \int_{d_{\text{crit}}}^{\infty} \frac{1}{d^p} \left(\frac{d}{r}\right)^m \Delta d \\ &= (p-1)N d_m^{p-1} \left(\frac{A_c}{\pi a \delta}\right)_r U_\infty \pi a \delta^{2-p} \int_{\left(\frac{d}{\delta}\right)_{\text{crit}}}^{\infty} \frac{1}{\left(\frac{d}{\delta}\right)^p} \frac{\left(\frac{d}{\delta}\right)^m}{\left[\left(\frac{d}{\delta}\right)_r\right]^m} \Delta\left(\frac{d}{\delta}\right) \\ &= (p-1)N d_m^{p-1} \left(\frac{A_c}{\pi a \delta}\right)_r U_\infty \frac{\pi a \delta^{2-p}}{\left[\left(\frac{d}{\delta}\right)_r\right]^m} \frac{1}{(p-m-1)\left(\frac{d}{\delta}\right)_{\text{crit}}^{p-m-1}} \end{aligned}$$

But $\delta \sim \frac{1}{\sqrt{U_\infty}}$ so that $U_\infty \delta^{2-p} \sim U_\infty^{p/2}$

If we set $\delta = \frac{K}{\sqrt{U_\infty}}$ then

$$F = \frac{K^{2-p}(p-1)N d_m^{p-1}}{(p-m-1) \left[\left(\frac{d}{\delta}\right)_r\right]^{p-1}} \left(\frac{A_c}{\pi a \delta}\right)_r \pi a \left[\frac{\left(\frac{d}{\delta}\right)_r}{\left(\frac{d}{\delta}\right)_{\text{crit}}}\right]^{p-m-1} U_\infty^{p/2} \quad (9)$$

It is seen that the generation rate depends on $U_\infty^{p/2}$ where p is the exponent in the particle size distribution function.

For $p = 5$, the patch generation rate varies as $U_\infty^{2.5}$. Further, if $N = 30$ particles/cm³ with $d_m = 16 \mu\text{m}$ and $s = 1.01$, the patch generation rate at $U_\infty = 50$ fps is 117 patches/sec for $(d/\delta)_{\text{crit}} = 0.4$ and 10 patches/sec for $(d/\delta)_{\text{crit}} = 1$. Accepting the concept of a particle as a moving roughness element, a critical particle diameter of the order of half the boundary layer thickness is considered to be quite plausible.

In any environment, the particle size distribution function may depend on time, depth and location. It should be apparent that a good determination of this function is needed in order to utilize the method presented in this section.

Another approach to estimating the generation rate of turbulent patches is to postulate some generation mechanisms and apply them in the calculation of the capture area. The present approach was taken to preserve the predictability of A_c , while putting all the assumptions into the efficiency function.

5. SUMMARY AND CONCLUDING REMARKS

In this report, particle trajectories around a submerged body, but outside its boundary layer, were calculated numerically. To the best of our knowledge, this is the first time that the Basset force and the virtual mass inertial force have been included in the computation of the particle motion in a non-uniform potential flowfield. For a submerged sphere, the capture area defined as the upstream cross-section area within which particles will enter the boundary layer, was determined from the particle trajectories. For particles that are nearly neutrally buoyant, the capture area, $A_c/\pi a\delta$ is independent of (d/δ) for small particle sizes. When $s = \rho_p/\rho_f$ is large, the normalized capture area decreases with (d/δ) when (d/δ) is small. However, it seems that at large (d/δ) , the computed normalized capture areas $A_c/\pi a\delta$ collapse together for all s and vary as $(d/\delta)^m$.

Based on the calculation of A_c , an heuristic estimation method to predict the generation rate of turbulent patches was developed. To bypass the unknown generation mechanisms, an empirical efficiency function, defined as the fraction of particles at certain diameter that generate turbulent patches, is proposed. To simplify the analysis, the efficiency function is assumed to be a unit step function equal to 1 for $d/\delta > (d/\delta)_{crit}$. For a particle size distribution, $n(d) \sim d^{-p}$, the generation rate, F , is shown to vary as $U_\infty^{p/2}$.

In order to apply the presented method to the estimation of the generation rates of turbulent patches in an arbitrary situation, the following three quantities must be either measured, calculated or assumed:

- $n(d)$, particle size distribution function
- $A_c\left(\frac{d}{\delta}\right)$, capture area
- $\eta\left(\frac{d}{\delta}\right)$, efficiency function

The distribution function $n(d)$ can, in fact, be measured on-site prior to a field test. Calculation of the capture area for arbitrary bodies can be troublesome, however, since the calculated flowfield must be known sufficiently well to enable reliable calculations of particle trajectories. This problem was averted in the case of the sphere because the flowfield around the sphere is known analytically. Finally, the efficiency factor which is tied intrinsically to the unknown generation mechanisms of turbulent patches would be most difficult to determine unambiguously.

It is, therefore, suggested that the presented method be viewed as an heuristic framework for evaluating drag perturbation and patch generation data. If the frequency of observed events, in fact, varies as $U_{\infty}^{p/2}$, then the capture area variations for a sphere can be used to provide estimates of critical particle size. Clearly, some experimental corroboration of the predicted trends is needed in order to justify further development of the method.

REFERENCES

- Carnahan, B., Luther, H.A. and Wilkes, J.O., Applied Numerical Methods, John Wiley & Sons, 1969.
- Gear, C.W., Numerical Initial Value Problems in Ordinary Differential Equations, Prentice-Hall, 1971.
- Hinze, J.O., Turbulence, McGraw-Hill, 1959.
- Michael, D.H., "*The Steady Motion of a Sphere in a Dusty Gas*," J. Fluid Mechanics, 31, Part 1, 1968.
- Morsi, S.A. and Alexander, A.J., "*An Investigation of Particle Trajectories in Two-Phase Flow Systems*," J. Fluid Mechanics, 55, Part 2, 1972.
- Odar, F. and Hamilton, W.S., "*Forces on a Sphere Accelerating in a Viscous Fluid*," J. Fluid Mech., 18, Part 2, 1964.
- Odar, F., "*Verification of the Proposed Equation for Calculation of the Forces on a Sphere Accelerating in a Viscous Fluid*," J. Fluid Mech., 25, Part 3, 1966.
- Schlichting, H., Boundary Layer Theory, McGraw-Hill, 1968.
- Symington, W.A., "*Analytical Studies of Steady and Non-Steady Motion of a Bubbly Liquid*," Ph.D. Dissertation, Cal. Inst. Tech., 1978.
- Yih, C.S., Fluid Mechanics, McGraw-Hill, 1969.

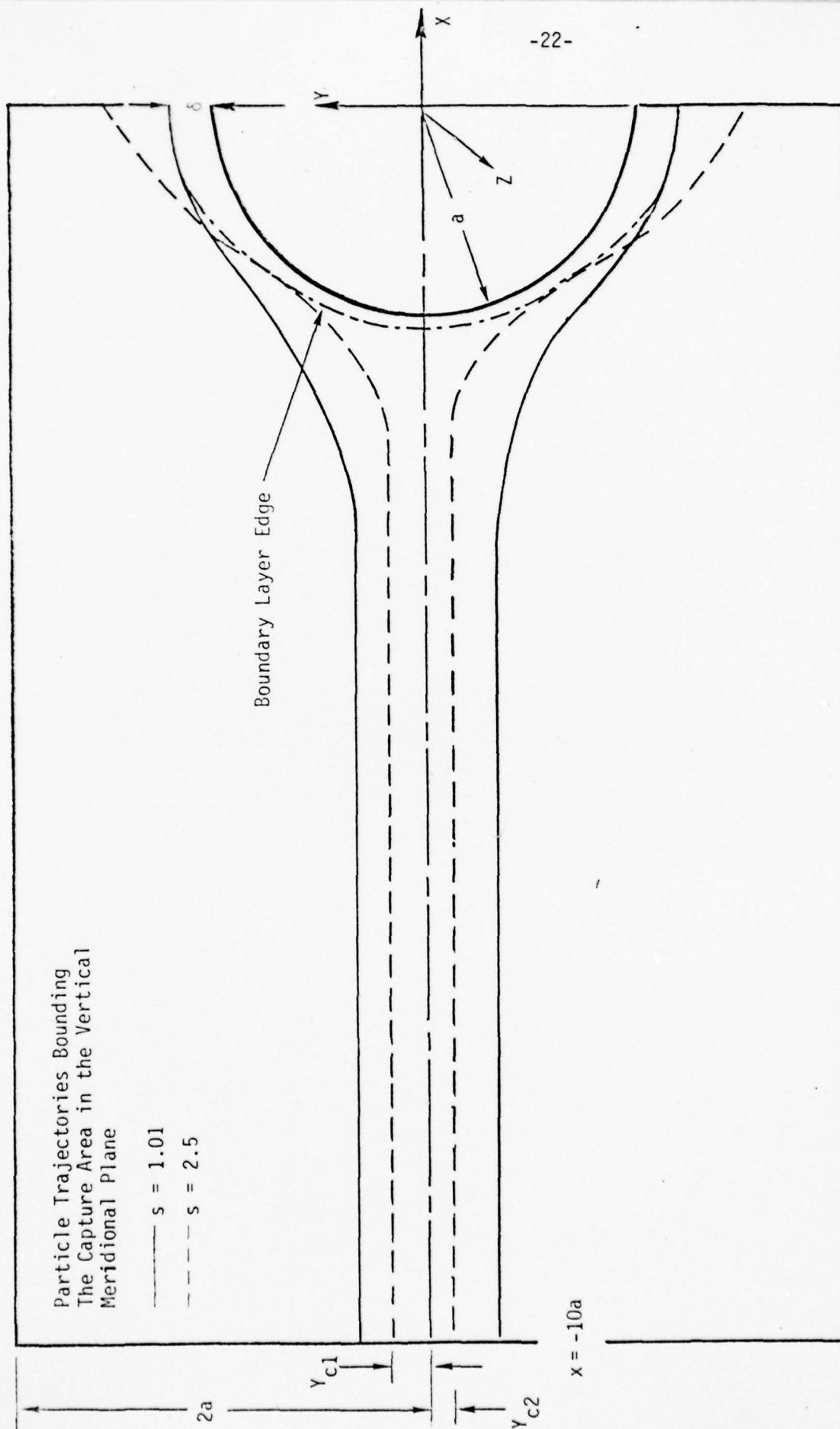


Figure 1. Schematic of Particle Trajectory Calculation in the Flowfield of a Submerged Sphere of Radius $a = 15.24$ cm (0.5 ft). Computations are Limited Inside the Area Encompassed by Heavy Lines. (The size of δ is exaggerated.)

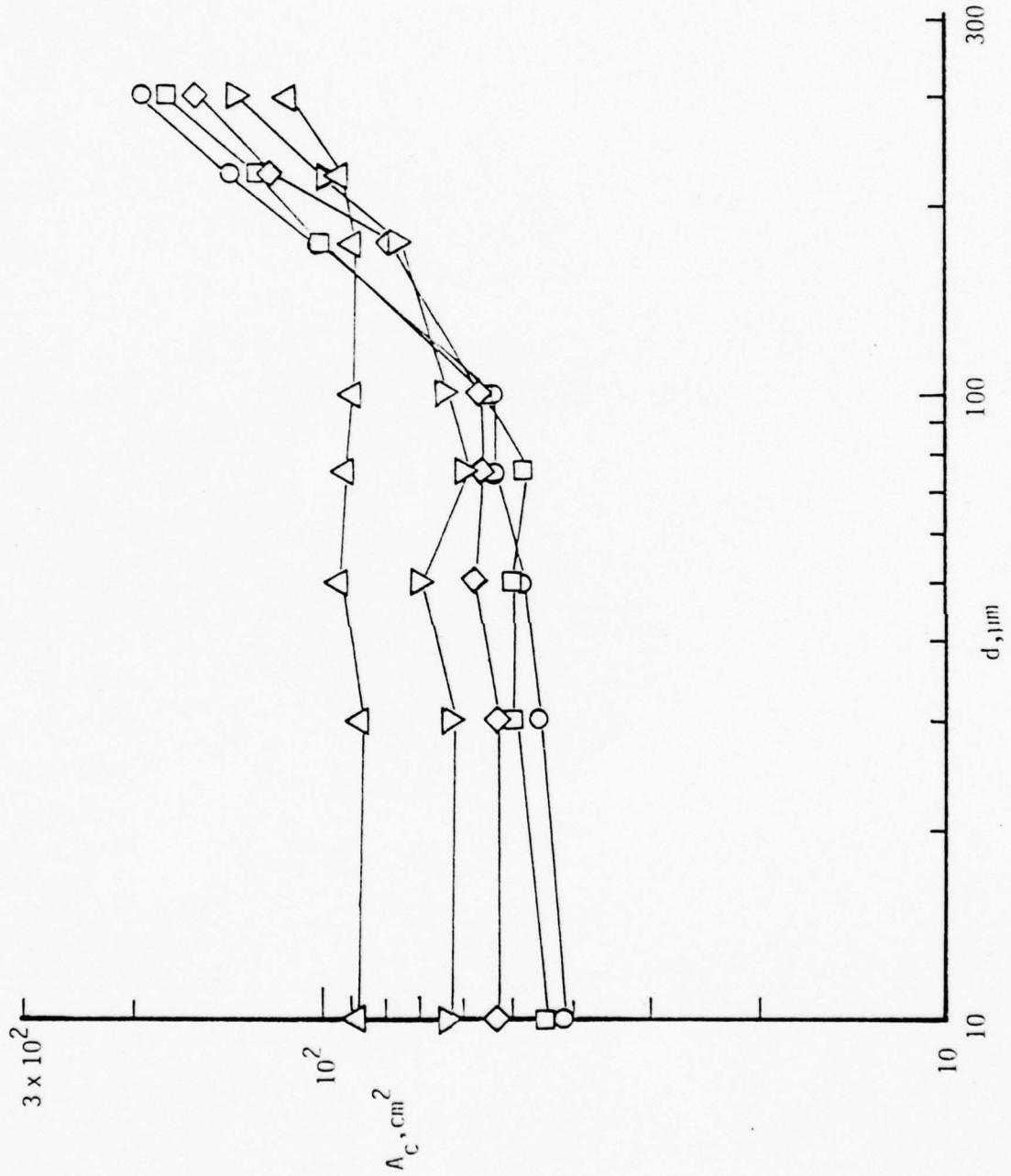


Figure 2. Capture Area versus Particle Diameter as a Function of U_∞ . $S = 1.01$.

\circ , 15.24 m/sec (50 ft/sec); \square , 12.19 m/sec (40 ft/sec); \diamond , 9.14 m/sec (30 ft/sec); ∇ , 6.1 m/sec (20 ft/sec); \triangle , 3.05 m/sec (10 ft/sec).

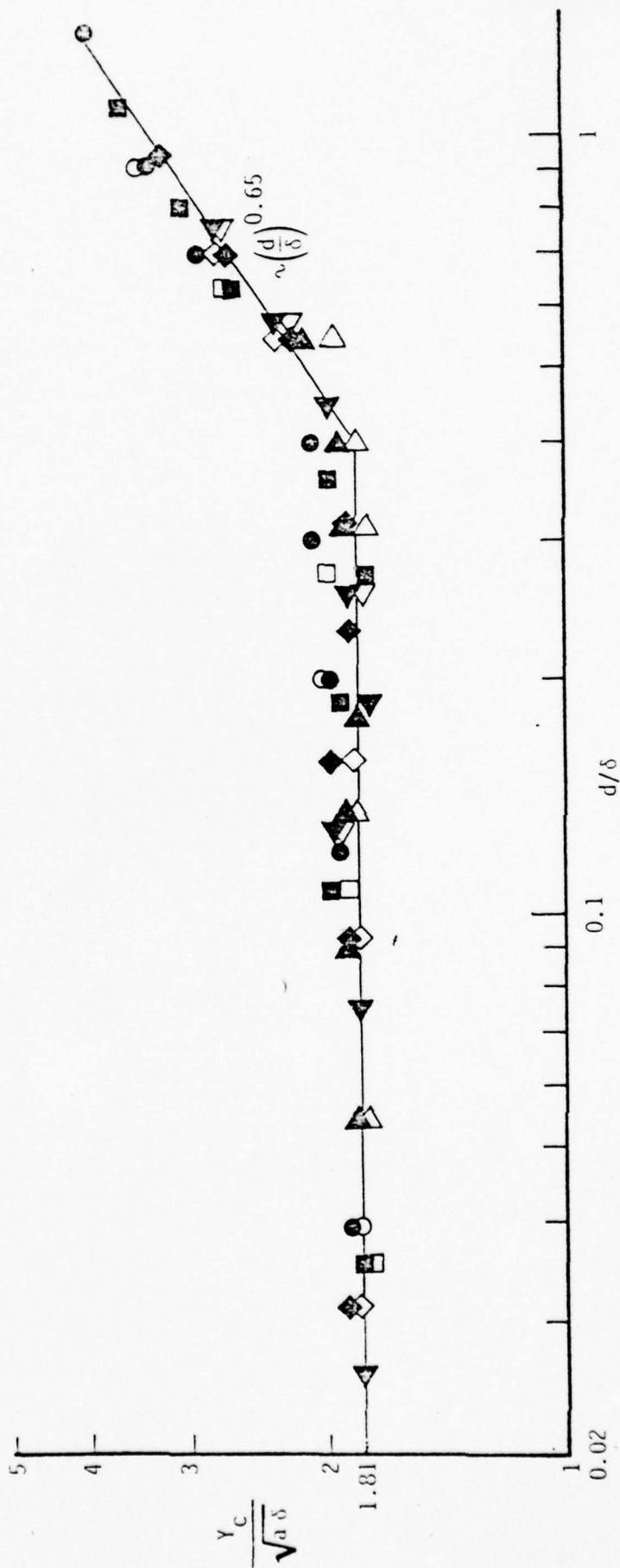


Figure 3. Capture Height as a Function of Particle Diameter. Open Symbol is Y_{c1} , Solid Symbol Y_{c2} .
 $s = 1.01$. O, 15.24 m/sec (50 ft/sec); □, 12.19 m/sec (40 ft/sec); ◇, 9.14 m/sec (30 ft/sec);
 △, 6.1 m/sec (20 ft/sec); ▽, 3.05 m/sec (10 ft/sec).

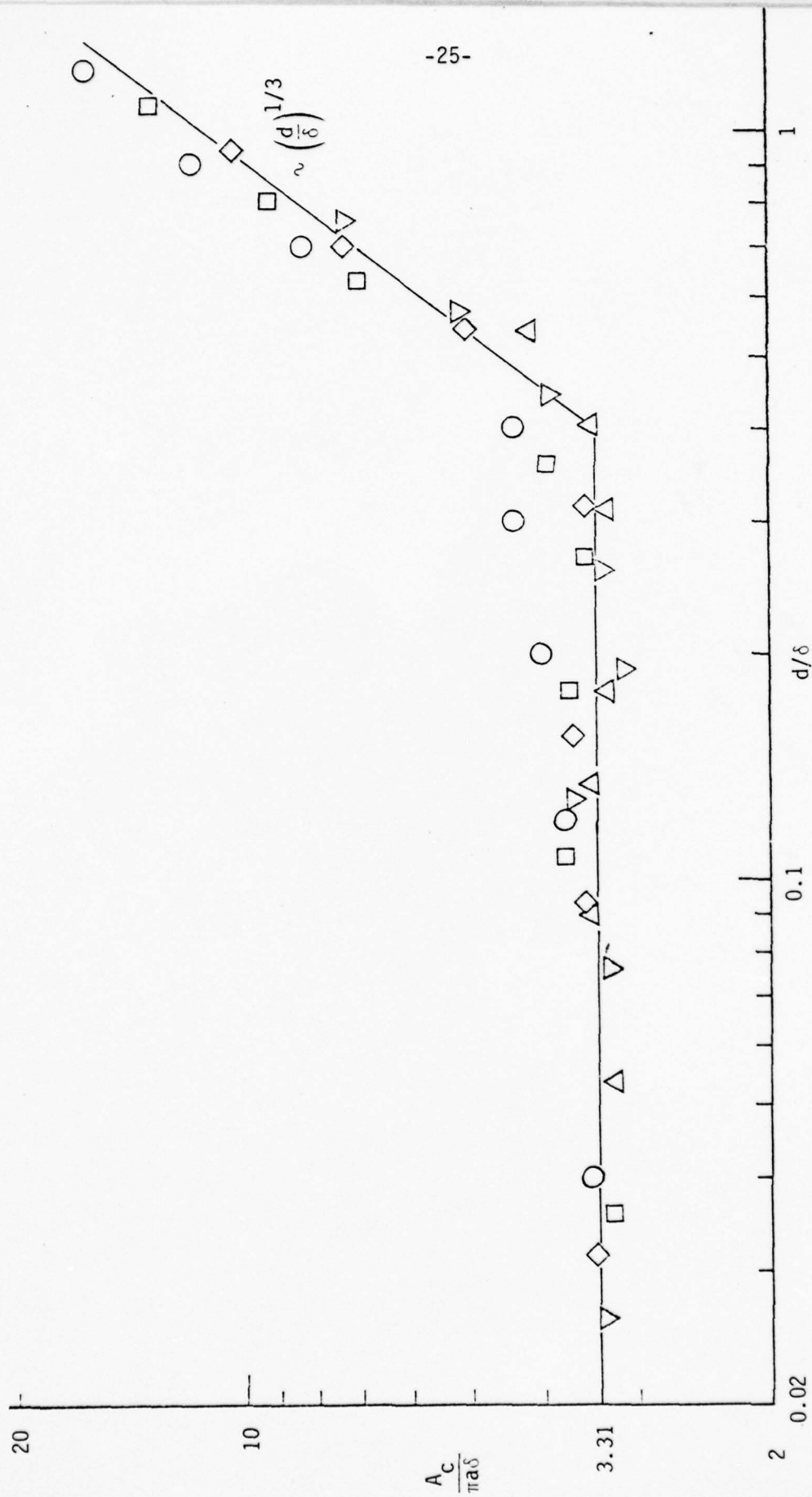


Figure 4. Normalized Capture Area as a Function of Particle Diameter. $s = 1.01$. \circ , 15.24 m/sec (50 ft/sec); \square , 12.19 m/sec (40 ft/sec); \diamond , 9.14 m/sec (30 ft/sec); ∇ , 6.1 m/sec (20 ft/sec); \triangle , 3.05 m/sec (10 ft/sec)

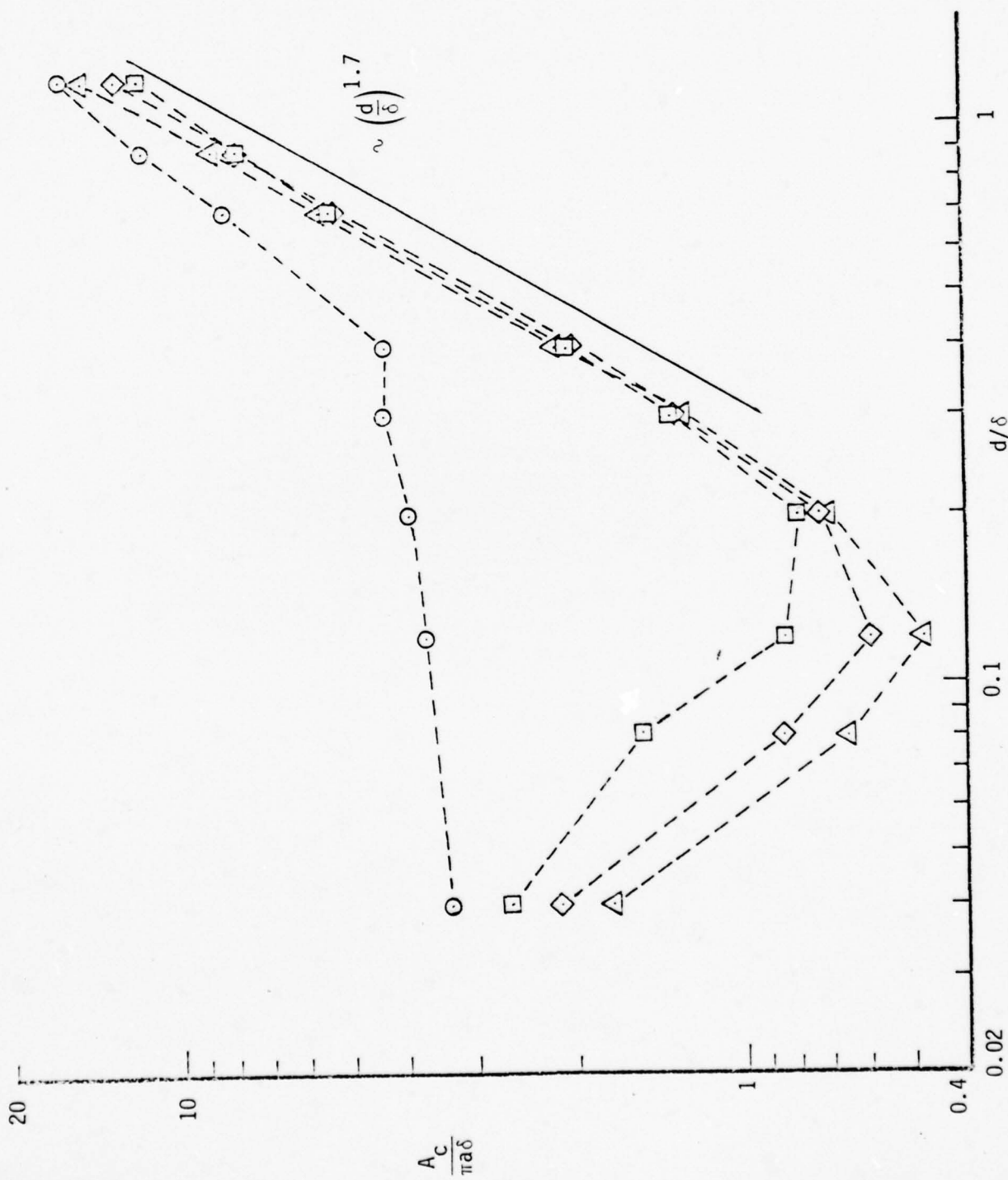


Figure 5. Normalized Capture Area as a Function of Particle Diameter. $U_\infty = 15.24$ m/sec (50 ft/sec) and Various Density Ratios. \bigcirc , $s = 1.01$; \square , $s = 1.5$; \diamond , $s = 2.0$; \triangle , $s = 2.5$.

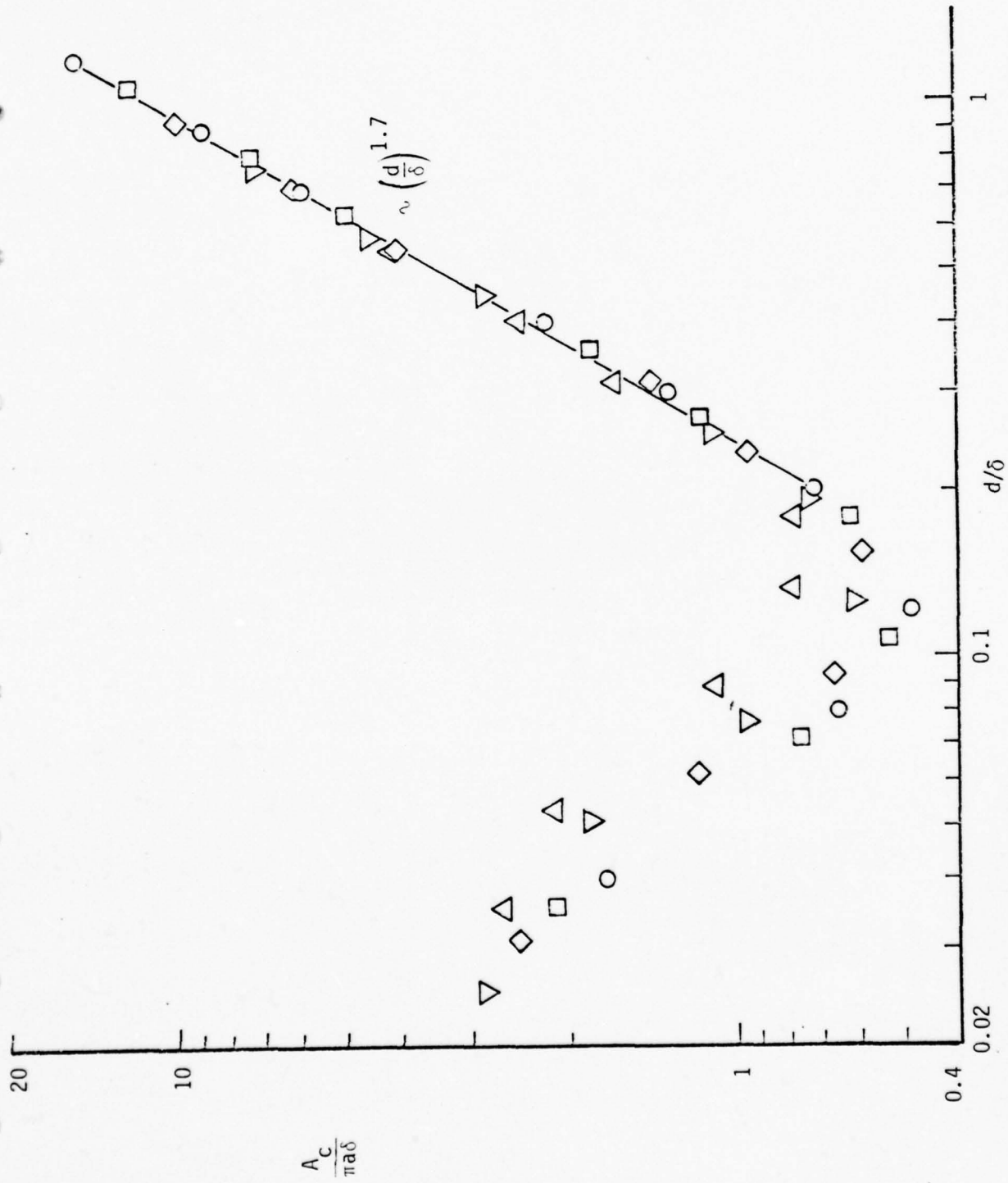


Figure 6. Normalized Capture Area as a Function of Particle Diameter. $s = 2.5$ and Various Speeds
 O, 15.24 m/sec (50 ft/sec); \square , 12.19 m/sec (40 ft/sec); \diamond , 9.14 m/sec (30 ft/sec);
 ∇ , 6.1 m/sec (20 ft/sec); \triangle , 3.05 m/sec (10 ft/sec).

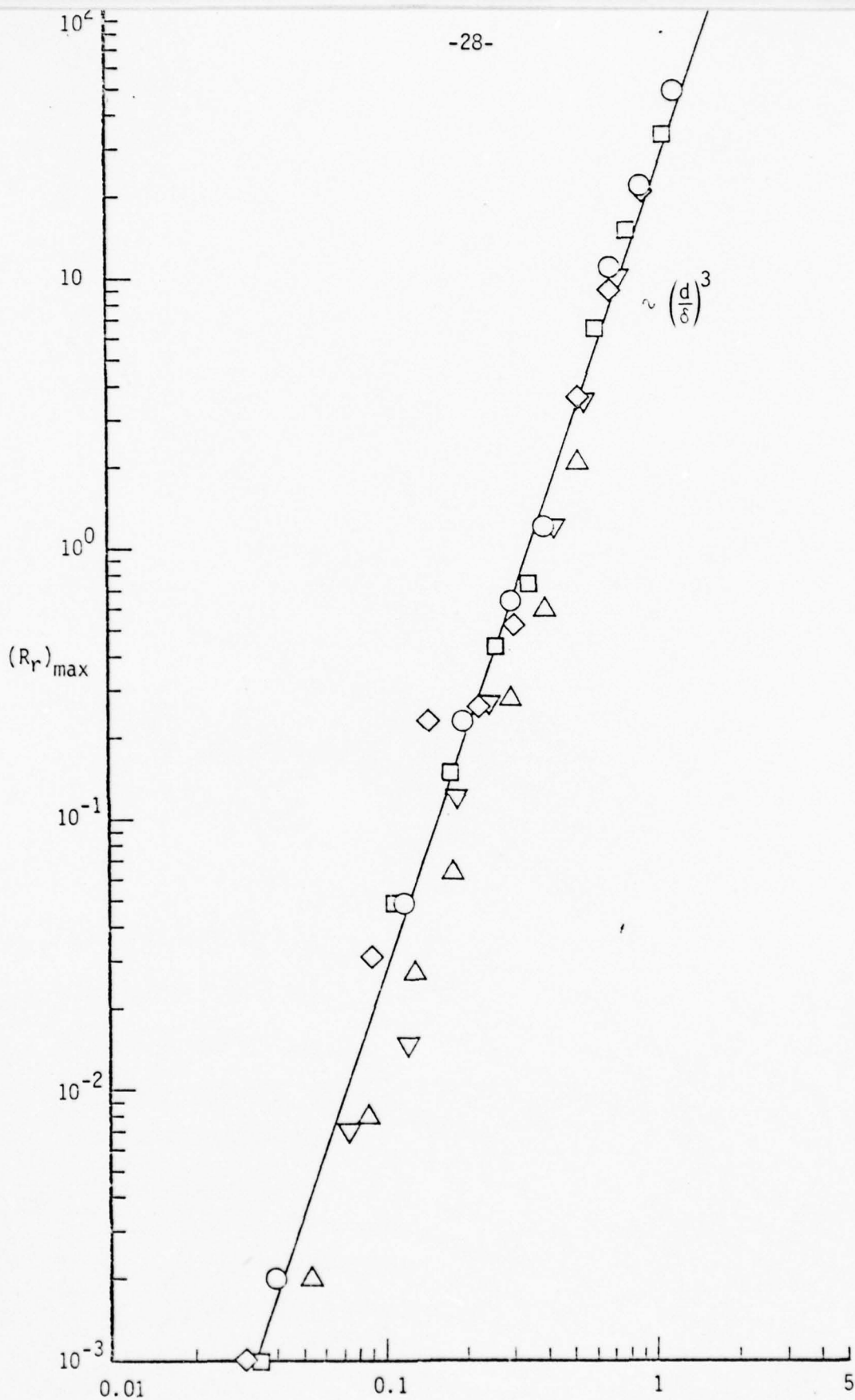


Figure 7. Maximum Relative Reynolds Number as a Function of Particle Diameter. $s = 1.01$
 ○, 15.24 m/sec (50 ft/sec); □, 12.19 m/sec (40 ft/sec);
 ◇, 9.14 m/sec (30 ft/sec); ▽, 6.1 m/sec (20 ft/sec); △, 3.05 m/sec (10 ft/sec)

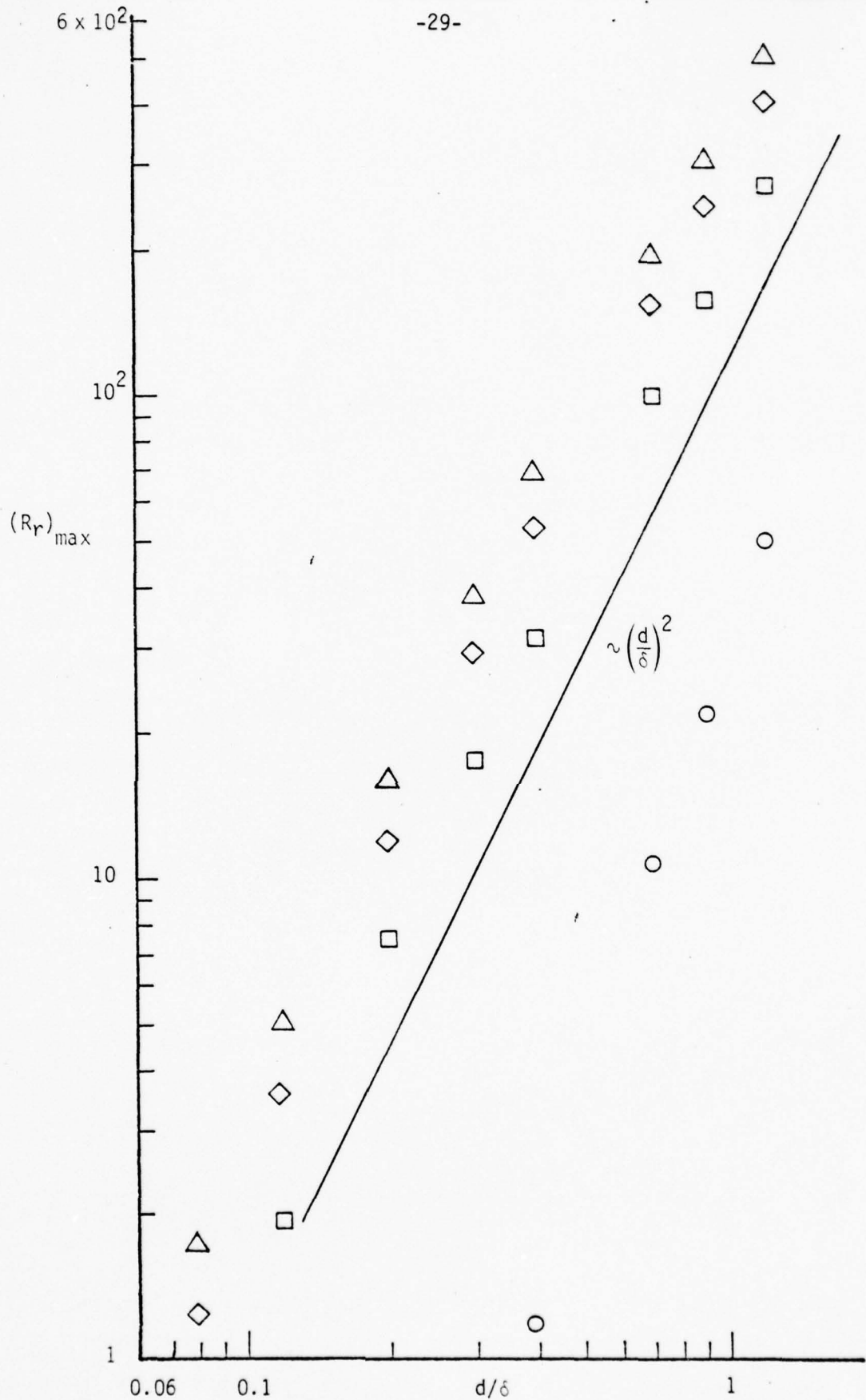


Figure 8. Maximum Relative Reynolds Number as a Function of Particle Diameter for Various Density Ratios. $U_{\infty} = 15.24$ m/sec (50 ft/sec).
 \bigcirc , $s = 1.01$; \square , $s = 1.5$; \diamond , $s = 2.0$; \triangle , $s = 2.5$.

APPENDIX A

DRAG COEFFICIENT OF A SPHERE
(from Morsi and Alexander, 1972)

$$C_D = A_1 + A_2 R_r^{-1} + A_3 R_r^{-2}$$

R_r	A_1	A_2	A_3
$R_r < 0.1$	0	24.0	0
$0.1 < R_r < 1.0$	3.69	22.73	0.0903
$1.0 < R_r < 10.0$	1.222	29.1667	-3.8889
$10.0 < R_r < 100.0$	0.6167	46.5	-116.67
$100.0 < R_r < 1000.0$	0.3644	98.33	-2778
$1000.0 < R_r < 5000.0$	0.357	148.62	-4.75×10^4
$5000.0 < R_r < 10000.0$	0.46	-490.546	57.87×10^4
$10000 < R_r < 50000.0$	0.5191	-1662.5	5.4167×10^6

APPENDIX B

SCALING PARAMETERS FOR PARTICLE TRAJECTORY CALCULATIONS

Michael (1968), in a study of the flow of a dusty gas past a sphere, found that the slip velocity between a dust particle and the flow, when normalized by the free stream velocity, scales with Stokes number, which was defined as

$$\left(\frac{s}{18}\right) \left(\frac{U_{\infty} a}{\nu}\right) \left(\frac{d}{a}\right)^2 .$$

In his study, the particle drag was described by the Stokes relation. He also considered the density ratio, s , to be much larger than unity so that Basset force and virtual mass terms were negligible. For $s \sim 1$, the Stokes number, which is essentially the ratio of the time scale over which the velocity of the dust particle adjusts to changes in the surrounding gas velocity to the flow time of the gas motion past the sphere, should have a different form. The Stokes number appropriate to our case can be obtained through careful examination of equation (3).

With the particle drag approximated by the Stokes relation, equation (3) is rewritten as

$$\begin{aligned} \frac{d\bar{u}}{dt} + \frac{36\nu}{(2s+1)d^2} \bar{u} + \frac{18\sqrt{\nu/\pi}}{(2s+1)d} \int_0^t \left[\frac{d\bar{u}}{d\tau} + (\bar{u} \cdot \nabla) \bar{V}_f \right] \frac{d\tau}{(t-\tau)^{1/2}} + (\bar{u} \cdot \nabla) \bar{V}_f \\ = \frac{2(s-1)}{2s+1} (\bar{V}_f \cdot \nabla) \bar{V}_f - \frac{2(s-1)}{2s+1} \bar{g} \end{aligned} \quad (B1)$$

Terms on the left hand side (LHS) are all related to \bar{u} and the terms on the right hand side (RHS) are independent of \bar{u} . In other words, equation (B1)

is a system of nonhomogeneous, first-order, integro-differential equations for \bar{u} , with the terms on the RHS as forcing functions. In order to estimate the relative magnitude of \bar{u}/U_∞ , a normalization scheme is required.

For the time being, we will leave out the integral term in the estimation of \bar{u}/U_∞ . Let $\bar{u} = \gamma U_\infty \bar{u}'$, $\bar{V}_f = U_\infty \bar{V}_f'$, $\bar{X} = a \bar{X}'$, and $t = \tau^* t'$, where \bar{u}' , \bar{V}_f' , \bar{X}' and t' are dimensionless quantities of order unity. γ characterizes the relative magnitude of the slip velocity to the free-stream speed. The above normalization implies $\nabla = \frac{1}{a} \nabla'$. All terms in equation (B1), except the integral term are now normalized according to the scheme and after all coefficients are divided by the coefficient of the first term on RHS and primes are dropped for convenience, equation (B1) becomes

$$C_1 \frac{d\bar{u}}{dt} + C_2 \bar{u} + C_4 (\bar{u} \cdot \nabla) \bar{V}_f = (\bar{V}_f \cdot \nabla) \bar{V}_f + C_5 \hat{k} \quad , \quad (B2)$$

where

$$C_1 = \frac{(2s+1) a \gamma}{2(s-1) U_\infty \tau^*} \quad ,$$

$$C_2 = \frac{18 \nu a \gamma}{(s-1) U_\infty d^2} \quad ,$$

$$C_4 = \frac{(2s+1) \gamma}{2(s-1)} \quad ,$$

$$C_5 = \frac{ga}{U_\infty^2} \quad .$$

The coefficient, C_5 , which is an inverse Froude number, is much smaller than unity even at the lowest vehicle speed considered which indicates that the gravitational effects on particle slip are negligible when compared to the effects of fluid inertia in the non-uniform flowfield.

There are two time scales involved in equation (B2) that can be estimated, without losing generality, by equating C_1 to C_2 and to C_4 , respectively. They are

$$\tau_1^* = \frac{(2s+1)d^2}{36 \nu} \quad \text{and}$$

$$\tau_2^* = \frac{a}{U_\infty}$$

It is clear that τ_1^* is the time scale on which the particle adjusts to the external flow by viscous force and τ_2^* is the characteristic time associated with the flow past the sphere. Their ratio, β ,

$$\beta = \frac{\tau_1^*}{\tau_2^*} = \frac{C_4}{C_2} = \frac{(2s+1)}{36} \left(\frac{U_\infty a}{\nu} \right) \left(\frac{d}{a} \right)^2 \quad (\text{B3})$$

is much smaller than unity. The numerical difficulty associated with this property is discussed in Appendix C. Since ϵ is small, the third term (of equation (B2)) on LHS is not important in assessing γ . Without losing generality, we can equate $C_2 = 1$ (which implies the balance of the first forcing term on RHS and the viscous term on LHS (in equation (B2)) to define γ :

$$\gamma = \frac{(s-1)}{18} \left(\frac{U_\infty a}{\nu} \right) \left(\frac{d}{a} \right)^2 \quad (\text{B4})$$

This definition of γ is very similar to the Stokes number of Michael, except for the factor involving s . They are, of course, approximately the same for $s \gg 1$. Figure B1 shows all the normalized capture areas plotted against $\gamma^{1/2}$. It is seen that all data with fixed s collapse rather well, but segregate according to the density ratio at large γ , indicating some other physical processes other than the viscous force is dominant. For $\gamma^{1/2}$ less than about 10^{-2} , the particles follow streamlines.

Now that we have a measure of the slip velocity without the Basset force. Based on this information we can now estimate the magnitude of the Basset force.

Applying the same normalization procedure as used to obtain equation (B2) to the Basset force term yields

$$C_3 \int_0^t \left[\frac{d\bar{u}}{dt} + \frac{\tau^* U_\infty}{a} (\bar{u} \cdot \nabla) \bar{V}_f \right] \frac{d\tau}{(t-\tau)^{1/2}} \quad (B5)$$

where

$$C_3 = \frac{9}{s-1} \sqrt{\frac{\nu}{\pi \tau^*}} \frac{\gamma a}{U_\infty d} \quad (B6)$$

In equations (B5) and (B6) we still have the liberty of choosing either of τ_1^* or τ_2^* to be τ^* . For either one of these two time scales, the sum of the bracketed terms in equation (B5) remains of order unity; however, C_3 has different values for the different values of τ^* chosen. These C_3 's are

$$C_3 = \frac{3}{\sqrt{(2s+1)\pi}} \quad \text{for } \tau^* = \tau_1^*, \text{ and} \quad (B7)$$

$$C_3 = \left[\frac{9\gamma}{2(s-1)} \right]^{1/2} = \frac{1}{2} \left(\frac{U_\infty a}{\nu} \right)^{1/2} \left(\frac{d}{a} \right) \quad \text{for } \tau^* = \tau_2^*.$$

The first C_3 is of order unity for the density ratios that we are considering, implying that the Basset force is as important as the inertial force of the fluid in determining \bar{u} in the short time scale. For the longer time scale, the second C_3 may also be of order unity when U_∞ and d are sufficiently large. This implies that the second C_3 is another important scaling parameter for the trajectory calculation.

In the text, the particle diameter is always normalized by δ at $\phi = 90^\circ$. This collapses the numerical results fairly well. This fact is, however, somewhat mystifying since δ does not appear in the scaling of terms in equation (3). However, d/δ can be written as

$$\frac{d}{\delta} = \frac{d}{2.46 \sqrt{\frac{a\nu}{U_\infty}}} = \frac{1}{2.46} \left(\frac{U_\infty a}{\nu} \right)^{\frac{1}{2}} \left(\frac{d}{a} \right)$$

which is functionally similar and numerically close to the second C_3 in equation (B7). Thus, the scaling of normalized capture area with d/δ is equivalent to scaling with $\gamma^{\frac{1}{2}}$ for a fixed s . For very small γ , we expect the viscous force is dominant so that γ (or $\gamma^{\frac{1}{2}}$) is the appropriate scaling parameter; for large d/δ , we expect the Basset force to be dominant, so that d/δ is the correct scaling parameter. The former statement is supported by Figure B1, and the latter statement is supported by Figure 5, where results of different density ratios are plotted together. For intermediate particle size, both viscous force and Basset force are important so that normalized capture areas do not scale with either γ or d/δ .

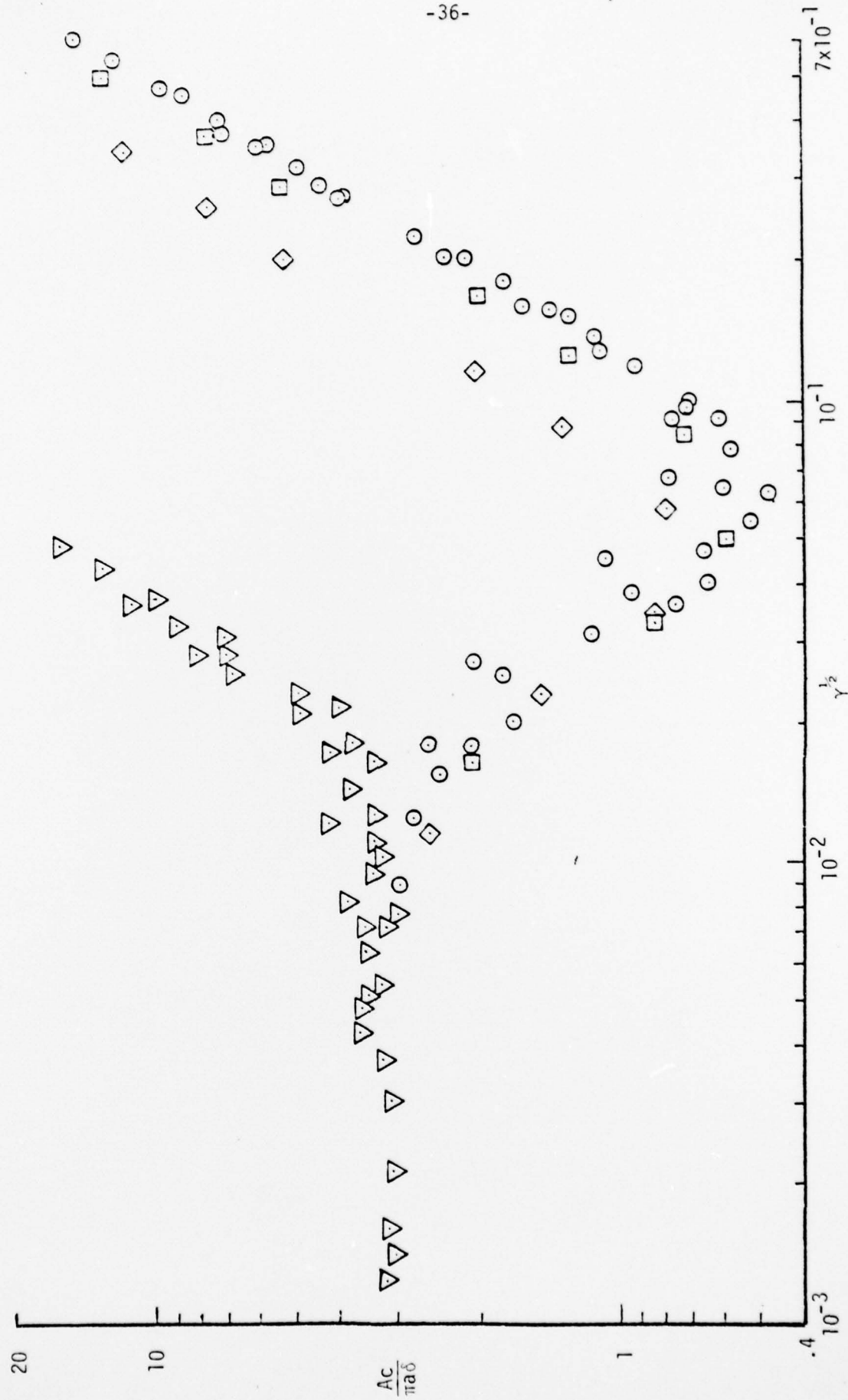


Figure B1: Capture area as a function of $\gamma^{1/2}$. ∇ , $s=1.01$; \square , $s=1.5$; \circ , $s=2.0$; \diamond , $s=2.5$. Data of $s=1.01$ and 2.5 are for all velocities. $U_\infty=15.24$ m/sec (50 m/sec) for $s=1.5$ and 2 .

APPENDIX C

NUMERICAL SOLUTION METHODS OF PARTICLE MOTION

C.1 Considerations for Numerical Formulation

The motion of a particle is described by its instantaneous velocity, \bar{V}_p , and location, \bar{X}_p . Instead of directly solving for \bar{V}_p , the relative velocity between the fluid and the particle, \bar{u} , is computed in order to improve numerical accuracy. The set of equations describing the particle motion is then,

$$\begin{aligned} \frac{d\bar{u}}{dt} + \frac{3}{2} \frac{1}{(2s+1)} \frac{C_D}{d} |\bar{u}| \bar{u} + \frac{18\sqrt{\nu/\pi}}{(2s+1)d} \int_0^t \left[\frac{d\bar{u}}{d\tau} + (\bar{u} \cdot \nabla) \bar{V}_f \right] \frac{d\tau}{(t-\tau)^{3/2}} \\ + \left(\bar{u} - \frac{2(s-1)}{2s+1} \bar{V}_f \right) \cdot \nabla \bar{V}_f + \frac{2(s-1)}{2s+1} \hat{g} = 0 \end{aligned} \quad (3)$$

for the relative velocity, and

$$\frac{d\bar{X}_p}{dt} = \bar{V}_f - \bar{u} \quad (4)$$

for the particle location.

Equations (3) and (4) are too complicated to be solved analytically and, thus, should be solved numerically. Before any numerical methods are chosen, the properties of equations (3) and (4) should be examined. Equation (3) has two kinds of numerical difficulty:

- (1) There are two time scales involved - one for local particle dynamics and the other for flows over the submerged body, and
- (2) the integrand of the Basset force term is singular at $\tau = t$.

Equation (B3) gives the ratio between the time scales in (1). For instance, given $s = 1.01$, $U_\infty = 10$ m/sec, $a = 0.15$ m, $d = 100$ μ m and $\nu = 1 \times 10^{-6}$ m²/sec

$$\beta = \frac{\tau_1^*}{\tau_2^*} = \frac{(2s+1)}{36} \left(\frac{U_\infty a}{\nu} \right) \left(\frac{d}{a} \right)^2 = 0.06 ,$$

where τ_1^* characterizes the particle dynamics and τ_2^* characterizes the flow over the submerged body. This example shows that there is a large disparity between the magnitude of τ_1^* and τ_2^* .

If a small enough time increment is chosen to resolve particle dynamics, it would take a great many steps to compute a particle's trajectory about the body. This operation is relatively expensive. On the other hand, when a large time increment is chosen, the numerical computation is very likely to be unstable. In numerical jargon, equation (3) is said to be "stiff." Stiff equations should be solved implicitly* to improve numerical stability for relatively larger time steps.

The singularity in the integrand of the Basset force term at $\tau = t$ can be resolved by approximating its bracketed part with a straight line in each time interval, and then integrate analytically within each interval. The essence of this method is shown in the relation,

$$\int_0^{t_n} \frac{f(\tau) d\tau}{\sqrt{t_n - \tau}} = \int_0^{t_{n-1}} \frac{f(\tau) d\tau}{\sqrt{t_n - \tau}} + h^{1/2} \left[\frac{2}{3} f_{n-1} + \frac{4}{3} f_n \right] , \quad (C1)$$

where h is the time increment and f_n is the value of f evaluation at t_n . The same process can be continued for as many time steps as needed to remove the steep gradient associated with the singularity. The remaining integral can be evaluated by any standard method.

* Implicit numerical methods usually mean that the difference equation of the corresponding differential equation is nonlinear and should be solved iteratively.

With the implementation of the above method to remove the singularity of the integrand, the improved Euler method coupled with the Newton-Ralphson method to solve nonlinear algebraic equations (Carnahan *et al.* 1969), is utilized to solve equation (3).

An explicit Euler method, an improved iterative Euler method, and 4th order and 6th order predictor-corrector methods have been tested to solve equation (4). Based on the accuracy of each method, the 4th order predictor-corrector method was chosen. More of the comparison between numerical methods is discussed later in this Appendix.

There are two reasons why equations (3) and (4) were solved separately, i.e., by different numerical methods. First, the computer cost was reduced in so doing. The improved Euler method used to solve equation (3) has low accuracy and, thus, should be iterated. Since computation cost increases with number of iterations and the number of operations in each iteration, it is more economical to utilize the 4th order predictor-corrector method to solve equation (4) with only one iteration. Secondly, the Newton-Ralphson method which is coupled to the improved Euler method to solve equation (3) would require the existence of the second order spatial derivatives of the velocity field. For an arbitrary body, the flowfield is given numerically. The spatial differentiation of the flowfield would introduce numerical difficulty in generating the flowfield. Since we would like to extend our calculation to arbitrary bodies in the future, the present approach of solving equations (3) and (4) by different methods was adopted.

The detailed numerical formulation is straightforward once the numerical methods are chosen. Interested readers are referred to Carnahan *et al.* (1969).

C2. Error Estimate and Time Increment of Numerical Computation

A numerical code was developed to integrate equations (3) and (4). The first check case was to calculate the trajectory for a particle released from rest in a still fluid. The parameters were carefully chosen so that the particle motion stayed in the Stokes' flow regime. The result was compared with the theoretical solution in Yih (1969). The agreement was excellent.

Since there is no analytic solution for the general case of particles moving in response to the flow around a body, we resorted to the trivial case of neutrally buoyant particles ($s=1$) released with no relative velocity and whose trajectories should be identical to streamlines. For the case of uniform flow over a sphere, the equation of the streamline is in the form

$$\left(\frac{r^2}{a^2} - \frac{a}{r} \right) \sin^2 \phi = Y_{\infty}^2 \quad (C2)$$

where r is the radial distance from the origin and Y_{∞} is the distance between the streamline and the centerline far upstream of the sphere. At the top of the sphere ($\phi = 90^\circ$), and when r is infinitesimally greater than a , i.e., $r = a + \zeta$, equation (C2) reduces to

$$Y_{\infty}^2 = 3a\zeta + O(\zeta^2) \quad (C3)$$

If the streamline is integrated by numerical methods, the fluid particle would reach ζ' (and $\zeta' \neq \zeta$) at the top of the sphere because of all the errors accumulated along the path. The error of the numerical computation is then defined as

$$\varepsilon (\%) = \frac{\zeta - \zeta'}{\zeta} \times 100 \quad (C4)$$

(In the context of computing the capture height, Y_{∞} and ζ are set to be Y_c and δ , respectively.) Then ϵ is used as the criterion to compare the error of various numerical methods and to determine the time increment.

Figure C1 shows ϵ versus time increment for various numerical methods used to solve equation (4). The δ at $U_{\infty} = 15.24$ m/sec was chosen for the computation of ϵ , and the corresponding Y_c was 10.73 mm. The explicit Euler method resulted in the worst accuracy. The improved Euler method already improved the accuracy considerably. The fourth and sixth order predictor-corrector methods, which are the best of all methods, had the same accuracy. Since the sixth order predictor-corrector method used more computer time, we decided to use the fourth order method. The time increment chosen was 4×10^{-4} sec which had an error of 16 percent. This error is only 0.027 percent in conventional definition when the denominator in equation (C4) is replaced by $(a + \zeta)$.

At this time increment, there were about 350 computational steps for each particle's trajectory in an external flow of 15.24 m/sec. When the external flow was slower, we increased the time increment so as to keep the number of computational steps to be around 350 in order to cut down computational cost while maintaining similar accuracy.

We also observed that ϵ is an oscillatory function of Y_{∞} , as shown in Figure C2. ϵ oscillates between 36% at $Y_{\infty} = 0.91$ cm to 5% at $Y_{\infty} = 1.55$ cm. Since the smallest Y_{∞} we are interested in is 1.07 cm (corresponding to $\delta = 0.267$ mm and $U_{\infty} = 15.24$ m/sec), we could set an upper bound for ϵ of 25 percent.

For neutrally buoyant particles, $Y_{c1} = Y_{c2} = Y_c$. Thus, the capture area A_c is linearly proportional to δ :

$$A_c = \frac{\pi}{4} (Y_{c1}^2 - Y_{c2}^2) = \pi Y_c^2 = 3\pi a \delta .$$

Consequently, the computational error of A_c is also described by ϵ , having an upper bound of 25 percent.

Since ϵ is always positive, indicating $\zeta > \zeta'$, i.e., the computed trajectory lies between the corresponding streamline and the sphere, this systematic error prompted us to apply an heuristic correction. We used an iterative scheme to search for Y_c . The criterion for stopping the search was when the distance between the particle center and the boundary layer edge was less than 10 percent of the boundary layer thickness. By requiring that the particle should always approach the boundary layer edge from outside, a certain amount of systematic error was offset by this correction. It is observed that the numerical error in computing A_c is about 10 percent, much less than the upper bound of 25 percent.

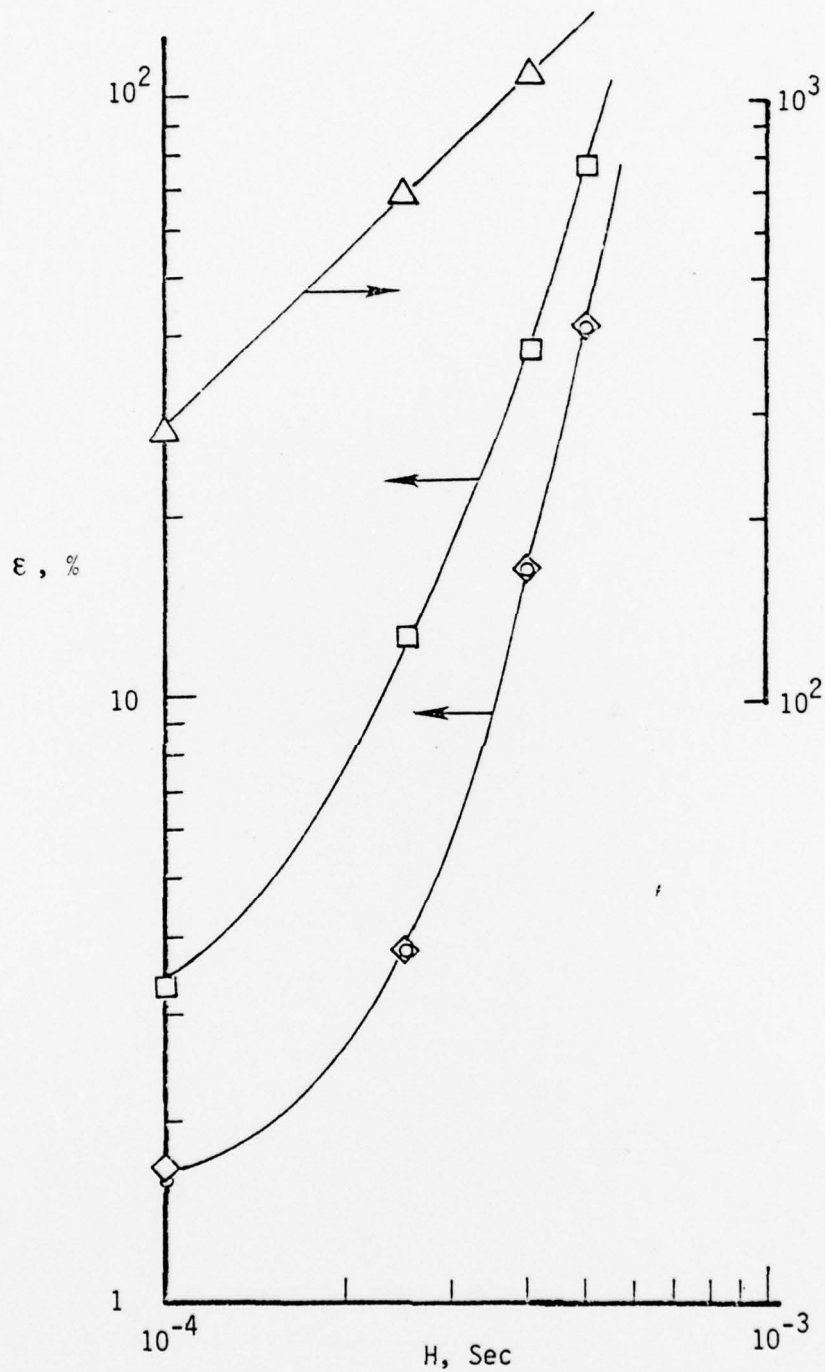


Figure C1. Percentage of Error for Different Numerical Methods
 Δ, Explicit Euler Method; □, Improved Euler Method;
 ○, Fourth Order Predictor-Corrector Method;
 ◇, Sixth Order Predictor-Corrector Method
 $U_{\infty} = 15.24 \text{ m/sec (50 ft/sec)}$, $d = 30 \text{ m}$, $s = 1.01$

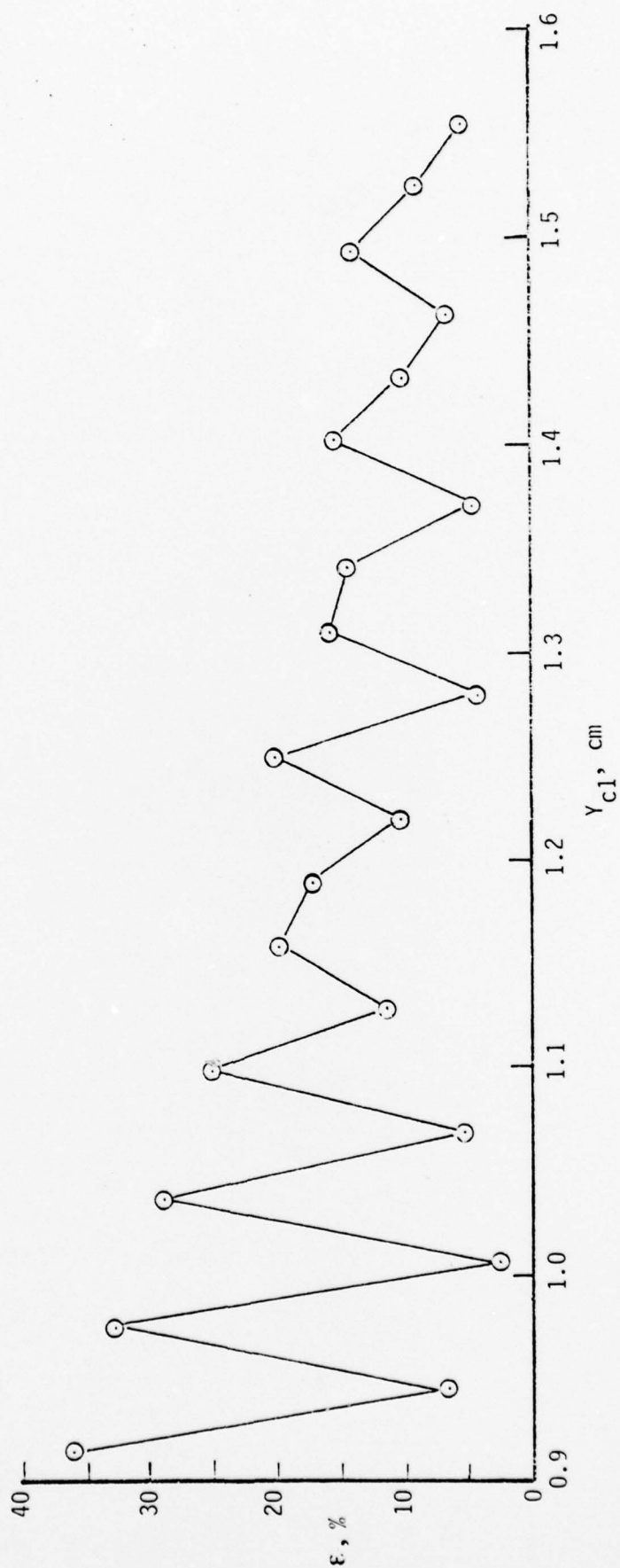


Figure C2. Percentage of Error versus Initial Particle Location. $U_{\infty} = 15.24 \text{ m/sec (50 ft/sec)}$, $d = 30 \mu\text{m}$, $s = 1.01$

APPENDIX D

EFFECTS OF BASSET FORCE AND VIRTUAL MASS

In the numerical code of calculating the particle's trajectory, there is a provision to incapacitate the contribution due to Basset force and virtual mass in order to study their individual or combined effects. The error associated with the exclusion of these terms is defined as

$$\text{error} = \epsilon = \frac{\delta - \delta'}{\delta} \times 100\%$$

Note that $(a+\delta)$ and $(a+\delta')$ are the intercepts of the particle trajectory with the Y axis for the same initial location upstream with or without Basset force and/or virtual mass.

Figure D-1 shows the percentage of error as a function of particle diameter for the case of $s = 1.01$, $U_{\infty} = 15.24 \text{ m/sec}$ (50 ft/sec) and $h = 4 \times 10^{-4} \text{ sec}$. For $d < 100 \mu\text{m}$, the error is less than 10%, which is comparable to the computation error. The error increases sharply to more than 2000% at $225 \mu\text{m}$, then it comes down to 70% at $300 \mu\text{m}$. It is observed that the effect of virtual mass is not as strong as that of Basset force. Since large particles are expected to disturb laminar boundary layer, the generation rate of turbulent patches would have a large error if Basset force and virtual mass are excluded from the particle trajectory computation.

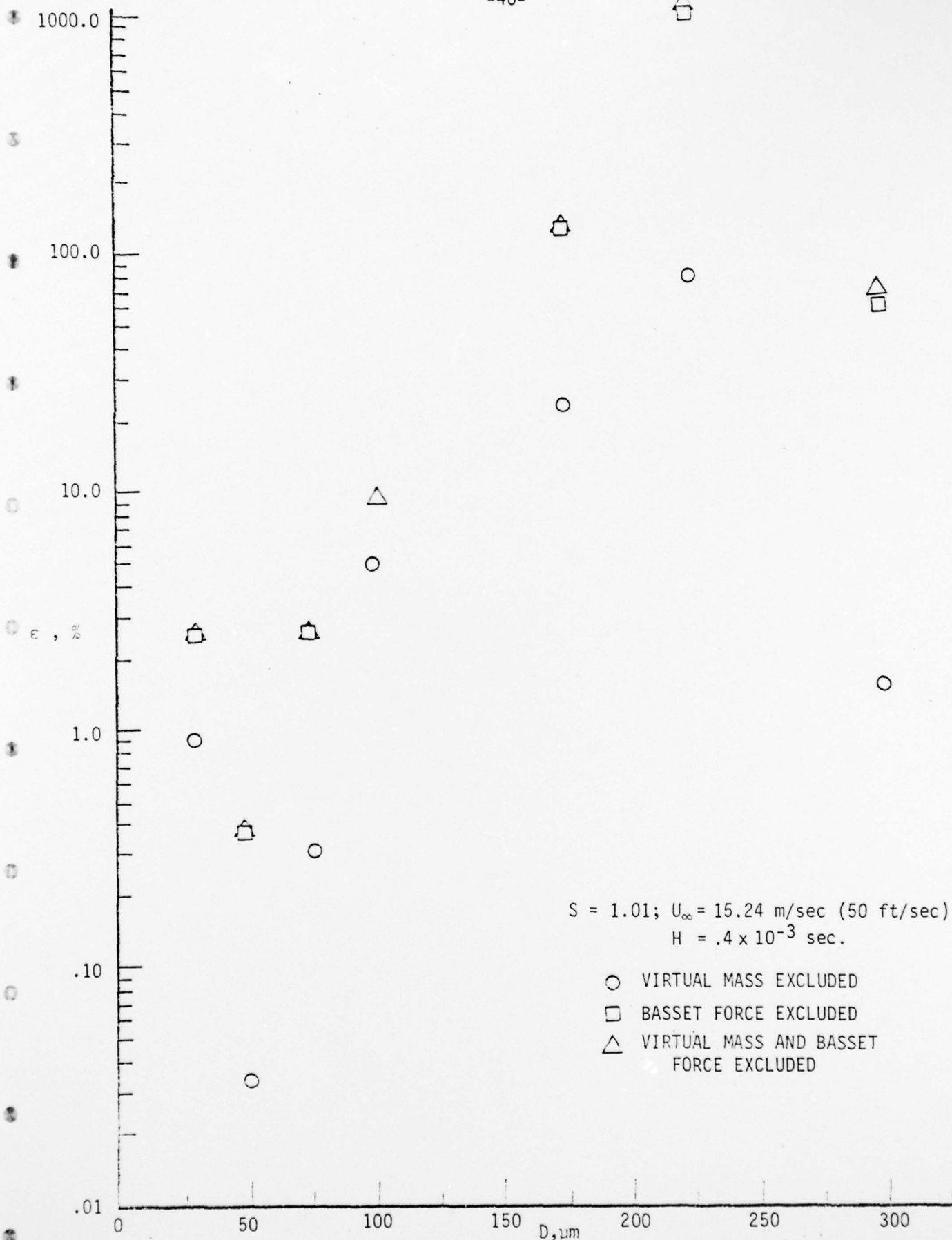


Figure D-1. Effect of Virtual Mass and Basset Force

DISTRIBUTION LIST FOR UNCLASSIFIED
TECHNICAL REPORTS ISSUED UNDER
CONTRACT N00014-77-C-0005 TASK NR 062-562

All addresses receive one copy unless otherwise specified.

Defense Documentation Center
Cameron Station
Alexandria, VA 22314 12 copies

Technical Library
David W. Taylor Naval Ship
Research and Development Center
Annapolis Laboratory
Annapolis, MD 21402

Library
Naval Academy
Annapolis, MD 21402

Dr. Philip A. Selwyn
DARPA/TTO
1400 Wilson Boulevard
Arlington, VA 22209

Office of Naval Research
Code 211
800 N. Quincy Street
Arlington, VA 22217

Office of Naval Research
Code 438
800 N. Quincy Street
Arlington, VA 22217 3 copies

NASA Scientific and Technical
Information Facility
P. O. Box 8757
Baltimore/Washington Inter-
national Airport
Maryland 21240

Dr. Steven J. Barker
Poseidon Research
11777 San Vicente Boulevard
Los Angeles, CA 90049

Mr. Roy Gulino
Westinghouse Electric Corp.
Oceanic Division
Box 1488
Annapolis, MD 21404

Librarian
University of California
Dept. of Naval Architecture
Berkeley, CA 94720

Library (Code 5641)
Dr. W. E. Cummins, Code 15
Dr. J. H. McCarthy, Code 1552
David W. Taylor Naval Ship Research
and Development Center
Bethesda, MD 20084 3 copies

Professor P. Leehey
Massachusetts Institute of Technology
Department of Ocean Engineering
Cambridge, MA 02139

Library
Naval Weapons Center
China Lake, CA 93555

Professor E. Reshotko
Case Western Reserve University
Div. of Chemical Engineering Science
Cleveland, OH 44106

Technical Library
Naval Weapons Surface Center
Dahlgren Laboratory
Dahlgren, VA 22418

Mr. Dennis Bushnell
NASA Langley Research Center
Langley Station
Hampton, VA 23365

Professor L. Landweber
Institute of Hydraulic Research
University of Iowa
Iowa City, IA 52242

Mr. Carl G. Jennings
Rockwell International Corp.
Autonetics Group
Anaheim, CA 92803

Distribution List (Cont.)

Fenton Kennedy Document Library
The Johns Hopkins University
Applied Physics Laboratory
Johns Hopkins Road
Laurel, MD 20810

Dr. S. Orszag
Cambridge Hydrodynamics, Inc.
54 Baskin Road
Lexington, MA 02173

Professor Tuncer Cebeci
California State University
Mechanical Engineering Dept.
Long Beach, CA 90840

Dr. T. D. Taylor
The Aerospace Corporation
P. O. Box 92957
Los Angeles, CA 90009

Lorenz G. Straub Library
St. Anthony Falls Hydraulic Lab.
University of Minnesota
Minneapolis, MN 55414

Library
Naval Postgraduate School
Monterey, CA 93940

Technical Library
Mr. Fred White, Code 36301
Mr. Richard Nadolink, Code 3635
Naval Underwater Systems Center
Newport, RI 02840 3 copies

Professor H. W. Liepmann
Graduate Aeronautical Laboratories
California Institute of Technology
Pasadena, CA 91109

Dr. Leslie M. Mack
Jet Propulsion Laboratory
California Institute of Technology
Pasadena, CA 91125

Technical Library
Dr. George L. Donohue, Code 6302
Dr. Michael M. Reischman, Code 6342
Dr. James Logan, Code 631
Naval Ocean Systems Center
San Diego, CA 92132 4 copies

Dr. Carl Gazley, Jr.
The Rand Corporation
1700 Main Street
Santa Monica, CA 90406

Librarian
Naval Surface Weapons Center
White Oak Laboratory
Silver Spring, MD 20910

Dr. D. R. S. Ko
Dynamics Technology, Inc.
3838 Carson Street, Suite 110
Torrance, CA 90503

Dr. Phillip S. Klebanoff
National Bureau of Standards
Mechanics Division
Washington, DC 20034

Dr. Robert J. Hansen
Naval Research Laboratory
Code 2627
Washington, DC 20375

Library (Code 09GS)
Dr. E. G. Liszka, Code 03421
Dr. Thomas E. Pierce, Code 03512
Mr. R. Manning, Code 395A
Naval Sea Systems Command
Washington, DC 20362 4 copies

Professor Blaine R. Parkin
Dr. G. C. Lauchle
Pennsylvania State University
Applied Research Laboratory
University Park, PA 16802 2 copies